Real-time phase-resolved ocean wave prediction in directional wave fields: Enhanced algorithm and experimental validation

I.-C. Kim, G. Ducrozet, F. Bonnefoy, Leroy Vincent, Y. Perignon

I.-C. Kim, G. Ducrozet, F. Bonnefoy, Leroy Vincent, Y. Perignon. Real-time phase-resolved ocean wave prediction in directional wave fields: Enhanced algorithm and experimental validation. Ocean Engineering, 2023, 276, pp.114212. 10.1016/j.oceaneng.2023.114212 . hal-04327969

Ocean Engineering 276 (2023) 114212

Contents lists available at ScienceDirect

Ocean Engineering

journal homepage: www.elsevier.com/locate/oceaneng

Real-time phase-resolved ocean wave prediction in directional wave fields: Enhanced algorithm and experimental validation

I.-C. Kim [*], G. Ducrozet, F. Bonnefoy, V. Leroy, Y. Perignon

Nantes Université, École Centrale Nantes, CNRS, LHEEA, UMR 6598, F-44000 Nantes, France

ARTICLE INFO

Dataset link: https://doi.org/10.5281/zenodo.7689781

Keywords:
Ocean waves
Phase-resolved model
Real-time prediction
Data assimilation
Directional wave
Wave tank experiments

ABSTRACT

This paper details a comprehensive study of deterministic real-time wave forecasting in directional seas. By using wave models on the basis of a Lagrangian description, a good balance was achieved between computational efficiency and model accuracy. Nevertheless, due to the highly non-uniform spatial distribution of data and the relatively small size of data in time inherent to remote optical measurements, the initial conditions are determined through an optimization process, which is computationally demanding, especially in multidirectional sea states. Accordingly, in order to offer a real-time system of wave prediction in the case of multidirectional waves, we propose a simplified and succinct assimilation method for the process of wave reconstruction. We also develop a three-dimensional spatio-temporal prediction zone where the future evolution of wave fields can be estimated based on wave measurements. Lastly, we outline a tank-scale experimental campaign conducted to mimic the measurements of a LIDAR in a real configuration. A comparison of model performances with the experimental observations shows that in a multidirectional approach, it is necessary to consider wave components in direction as well as in frequency to achieve nearly the same accuracy as for unidirectional seas.

1. Introduction

One of the central problems in the study of marine science and ocean engineering is the real-time prediction of the ocean wave surface. It is of great importance concerning the operations of surface vessels (Grilli et al. 2011, Nouguier et al. 2013, Kusters et al. 2016,?, Dannenberg et al. 2010), ocean wave energy harvesting systems (Li et al. 2012, Previsic et al. 2021), and the design of marine structures such as floating wind turbines (Ma et al., 2018). In particular, the optimal control of issues such as load mitigation on offshore floating wind turbines requires sufficiently accurate real-time forecasting of the ocean wave surface. This is the framework of the European H2020 FLOATECH and French ANR CREATIF projects, that funded the present study.

Phase-averaged models based on an energy balance equation (e.g., SWAN, Booij et al. 1999) provide ocean wave prediction in terms of wave energy density. Since the models describe the average properties of the ocean wave field without phase information (or a history of phase correlations) and implement a crude and overly-simplified parameterization for nonlinear wave–wave interactions, they have inherent difficulties in capturing more accurate and detailed nonlinear processes. As an alternative, phase-resolved models can describe the instantaneous state of ocean wave motion and the statistical properties (i.e., higher-order moments) in relation to nonlinear surface wave dynamics.

In an attempt to predict the ocean surface wave elevation from spatio-temporal measurements, a number of authors have used data sets obtained by LIDAR (Light Detection and Ranging) cameras (e.g., Grilli et al. 2011, Nouguier et al. 2013, Kabel et al. 2019, Desmars et al. 2020). We note that there are currently no commercial operating solutions for this technology. Similar effort toward the representation of the ocean wave field has been made with X-band radars (or microwave radars): examples include Hilmer and Thornhill (2015), Kusters et al. (2016), Naaijen et al. (2018), Klein et al. (2020), and Zhang et al. (2022). When the LIDAR camera or X-band radar operating at grazing angles is mounted upon the structure or vessel, both are subject to a spatially uneven distribution of measurement points. Namely, the density of points becomes sparse with increasing distance from the vessel-mounted instrument. In addition, shadowing effects caused by spatial gaps behind the illuminated wavefronts lead to a randomly non-uniform spatial grid over the domain. In order to circumvent the shadowing effects, the spatio-temporal data sets can be used to yield the ocean surface surrounding the camera in order to rapidly detect the points under shadows. However, it is more computationally demanding

---

[*] Corresponding author.
E-mail address: inchul.kim@ec-nantes.fr (I.-C. Kim).

https://doi.org/10.1016/j.oceaneng.2023.114212
Received 16 December 2022; Received in revised form 6 March 2023; Accepted 13 March 2023

to reconstruct phase-resolved random wave fields based on spatio-temporal data (Grilli et al. 2011, Nouguier et al. 2013, Desmars et al. 2018, 2020). On the other hand, for X-band radars, one can avoid shadowing effects by employing a 'shadowing mask' in the process of inversion. In addition to the highly non-uniform gaps between measurements in space, a relatively small number of aperiodic observations in time require a post-processing technique (e.g., remapping method, Belmont et al. 2007) to Fourier transform the wave field into the frequency domain.

In many marine engineering applications, it is often sufficient to use linear wave propagation models for a phase-resolved wave prediction (Hilmer and Thornhill 2015, Wijaya et al. 2015, Naaijen et al. 2018, Al-Ani et al. 2020). However, for a long-term forecast or nonlinear irregular sea states with a non-negligible wave steepness, nonlinear wave effects (particularly the nonlinear dispersion relation) are fairly significant; nonlinear models should become more appropriate to provide accurate real-time wave predictions (Guérin et al., 2019). Hence, in order to achieve proper representations of nonlinear wave fields, several attempts have been made to employ High-Order Spectral (HOS) models in the reconstruction and propagation algorithms (Wu 2004, Blondel et al. 2010, Köllisch et al. 2018, Qi et al. 2018a). Despite highly accurate phase-resolved descriptions of wave fields, the approaches based on the HOS method suffer from a much more demanding computational cost, particularly in the step of higher-order assimilation/reconstruction.

Since Nouguier et al. (2009) formulated the Choppy Wave Model (CWM) on the basis of Lagrangian analysis, CWM has been implemented to ease the computational demands while maintaining the model accuracy somewhat resulting from the inclusion of nonlinearity (Grilli et al. 2011, Nouguier et al. 2013). In comparison to the Eulerian approach, the Lagrangian model at the equivalent order appears to be particularly attractive for the study of waves in severe sea states and higher-order wave properties such as surface slope and skewness (Pierson, 1961). This is because the Lagrangian wave model involves higher-order nonlinear properties than its counterpart based on Eulerian expansion. Later, Nouguier et al. (2015) developed a second-order CWM (CWM2) to incorporate the higher nonlinear wave properties, and Guérin et al. (2019) subsequently proposed the Improved Choppy Wave Model (ICWM), which extended CWM2 by introducing a modified nonlinear dispersion relation with corrected reference particle location. More recently, Desmars et al. (2020) demonstrated that using ICWM in the data assimilation (or reconstruction; 'nowcast') and wave propagation (or prediction; 'forecast') provides an improvement as ICWM accounts for nonlinear wave properties when it comes to phase shift (or wave celerity).

In the present study, we extend the approach of Desmars et al. (2020), which investigated the case of unidirectional waves (or long-crested waves), to the case of multidirectional waves (or short-crested waves). In the case of multidirectional waves, the computational burden is obviously expected to be even higher because of the many additional wave components and measurements required to incorporate directional spreading in the model and data sets, respectively. Accordingly, we suggest an enhanced assimilation procedure in the process of reconstruction, which is anticipated to lead to a significant reduction in the calculation effort. Besides the increasing computational load, the inclusion of directional components in the wave field renders the nonlinear wave–wave interactions more complex and richer as it accounts for all the combinations between aligned and non-aligned wave vectors in the two-dimensional wave field in space, which is likely to be responsible for redistributing the energy over a wide range of directions (Janssen et al. 2006, Nouguier et al. 2015). Therefore, we examine the effects of nonlinearity included in ICWM on solving the propagation of multidirectional waves.

The process of phase-resolved real-time wave prediction involves determining the prediction zone in the spatio-temporal domain based on the prescribed wave field in terms of frequency and direction (Wu 2004, Naaijen et al. 2014, Qi et al. 2018b). Recently, Qi et al. (2018b) generalized the theoretical prediction zone by considering a variety of scenarios such as a single measurement or multiple measurements which are fixed or moving for either unidirectional or multidirectional cases. Similarly, we address problems of determining the prediction zone for the given situation where the measured points are acquired by a vessel-mounted sensor.

In the following, Section 2 presents an explanation of the wave models for nowcasting and forecasting. In particular, a simplified and more efficient assimilation method during nowcast is proposed in Section 2.2. The analysis of experimental data and the study of the prediction zone are given in Sections 3 and 4, respectively. The wave prediction algorithms are validated against dedicated tank-scale experiments. Multi-directional sea-states are generated, which are measured thanks to a network of wave gauges mimicking the measurements of a LIDAR in a full-scale real configuration. Section 5 describes the numerical modeling setups selected in our simulations. Section 6 presents the comparison between models as well as the comparison with reference experimental data. Finally, conclusions are given in Section 7.

2. Methods

The algorithms for real-time phase-resolved ocean wave prediction are composed of two steps: (1) data assimilation to reconstruct the initial wave conditions or wave amplitude parameters on the basis of observations; (2) wave propagation to simulate wave surfaces over a certain zone in the space–time domain (or prediction zone).

2.1. *Wave models*

Following the approach of Desmars et al. (2020), we chose ICWM to achieve a good compromise between numerical stability, efficiency, and model accuracy in terms of higher-order wave properties for the three-dimensional descriptions of sea surfaces in space and time. In addition to ICWM, two models are considered to evaluate the effect of nonlinearity in ICWM: one based on linear wave theory (LWT); the other based on linear wave theory, but with a corrected dispersion relationship (LWT-CDR).

2.1.1. *LWT*

A Cartesian coordinate system $(x, y, z) = (\mathbf{r}, z)$ is selected, with z taken positive vertically upwards from the still water level. For inviscid, incompressible, and irrotational fluid, the linearized water wave boundary problem with respect to wave steepness yields the free surface elevation:

$$\begin{aligned} \eta^{\mathrm{LWT}}(x, y, t) &= \sum_{n=1}^{N} [a_n \cos\psi_n + b_n \sin\psi_n] \\ &= \sum_{n_\omega=1}^{N_\omega} \sum_{n_\theta=1}^{N_\theta} [a_{(n_\omega,n_\theta)} \cos\psi_{(n_\omega,n_\theta)} + b_{(n_\omega,n_\theta)} \sin\psi_{(n_\omega,n_\theta)}] \end{aligned} \tag{1}$$

where subscript n indicates the nth wave component, which is defined as a pair of $n = (n_\omega, n_\theta)$; n_ω and n_θ denote the n_ωth wavenumber component (or quasi-frequency component) and the n_θth direction component, respectively. The total number of wave components is $N = N_\omega \times N_\theta$ and the wave amplitude parameters (a_n, b_n) are given by a combination of the complex amplitude A_n and the phase φ_n:

$$(a_n, b_n) = (A_n \cos\varphi_n, A_n \sin\varphi_n) \tag{2}$$

and the linear phase function in space and time is given:

$$\psi_n = \mathbf{k}_n \cdot \mathbf{r} - \omega_n t = k_{n_\omega} \cos\theta_{n_\theta} x + k_{n_\omega} \sin\theta_{n_\theta} y - \omega_{n_\omega} t \tag{3}$$

in which the wavenumber vector $\mathbf{k}_n$ consists of the wavenumber k_{n_ω} and the propagating direction θ_{n_θ} with respect to the $+x$-direction (where the unit wave vector is $\hat{\mathbf{k}}_{n_\theta} = \mathbf{k}_n / k_{n_\omega} = (\cos\theta_{n_\theta}, \sin\theta_{n_\theta})$):

$$\mathbf{k}_n = k_{n_\omega} \hat{\mathbf{k}}_{n_\theta} = (k_{n_\omega} \cos\theta_{n_\theta}, k_{n_\omega} \sin\theta_{n_\omega}) \tag{4}$$

where the wavenumber k_{n_ω} and the wave angular frequency ω_{n_ω} satisfy the linear dispersion relation in deep water $\omega_{n_\omega}^2 = gk_{n_\omega}$, where g is the gravitational acceleration. Here, we assumed deep water to develop the models for conciseness and simplicity, but the extension to a finite water depth is readily obtainable.

2.1.2. ICWM

Based on the Lagrangian expansion on the ocean surface, Nouguier et al. (2009) developed CWM, which allows for efficient simulation of nonlinear ocean surfaces. However, a significant drawback of CWM due to the lack of nonlinearity in its celerity is its limited applicability to sea states with weak nonlinearity. Therefore, we here apply ICWM derived from the second-order Lagrangian expression, retaining some higher-order features (third-order Stokes theory) at the same numerical cost as CWM (Guérin et al., 2019).

The Lagrangian dynamical formulation is not suitable for most applications, since wave information is usually taken in the form of time series from stationary gauges or at irregularly distributed locations in an Eulerian coordinate system. To utilize the wave information based on the Eulerian system in Lagrangian-based models, it is desirable to transform the Lagrangian model into an approximate Eulerian model by formulating the particle displacement with respect to the instantaneous location. This approximation is based on the assumption that the second-order moment of wave power spectral density is negligible compared to the other quantities in the process of wave prediction algorithm (Grilli et al. 2011, Nouguier et al. 2013, Desmars et al. 2020). The reader is referred to Guérin et al. (2019) and Desmars et al. (2020) for the full derivation of surface elevation at its instantaneous plane (i.e., $\mathbf{r}$) from water particle functions in time and the reference locations. The explicit form of free surface elevation by ICWM is

$$\eta^{\text{ICWM}}(x, y, t) = \sum_{n=1}^{N} [a_n \cos \Psi_n + b_n \sin \Psi_n + \frac{1}{2}({a_n}^2 + {b_n}^2)k_n] \tag{5}$$

where the nonlinear phase function Ψ_n involves the nonlinear phase shift (i.e., summation in Eq. (6)) and Stokes drift $\mathbf{U}_{s0}$:

$$\Psi_n = \mathbf{k}_n \cdot [\mathbf{r} - \sum_{i=1}^{N} \hat{\mathbf{k}}_i(-a_i \sin \tilde{\psi}_i + b_i \cos \tilde{\psi}_i)] - \tilde{\omega}_n t \tag{6}$$

$$\mathbf{U}_{s0} = \sum_{n=1}^{N} ({a_n}^2 + {b_n}^2)\omega_n \mathbf{k}_n \tag{7}$$

in which the corrected wave angular frequency with Stokes drift is $\tilde{\omega}_n = \omega_n + \frac{1}{2}\mathbf{k}_n \cdot \mathbf{U}_{s0}$ where a tilde superscript denotes any function modified with Stokes drift. Hence, the modified nonlinear phase function $\tilde{\psi}_n$ includes only Stokes drift $\mathbf{U}_{s0}$:

$$\tilde{\psi}_n = \mathbf{k}_n \cdot \mathbf{r} - \tilde{\omega}_n t \tag{8}$$

We note that the last term in Eq. (5) is introduced to have the zero-mean sea level.

2.1.3. LWT-CDR

As in Desmars et al. (2020), we also consider the resulting ocean wave surfaces simulated by the linear wave theory with the corrected dispersion relation (LWT-CDR):

$$\eta^{\text{LWT-CDR}}(x, y, t) = \sum_{n=1}^{N} [a_n \cos \tilde{\psi}_n + b_n \sin \tilde{\psi}_n] \tag{9}$$

which quantifies separately the effect of the nonlinear phase shift and Stokes drift in the nonlinear phase function Ψ_n for the multidirectional cases. For the unidirectional cases reported in Desmars et al. (2020), the improvement of ICWM in the prediction of surface elevation is mainly attributed to Stokes drift rather than the nonlinear phase shift although ICWM better accounts for some properties related to the wave shape than LWT-CDR for moderate or severe wave conditions.

2.2. Data assimilation

Assuming that the amplitudes and wave phases (i.e., a_n and b_n) over the prespecified spectrum are unchanged in time and space, we are able to estimate the optimal wave amplitude parameters through the model-based inversion from the ocean surface measurements $\bar{\eta}$. As in previous studies such as Blondel et al. (2010), we here choose a variational assimilation, which uses all the spatio-temporal observations to minimize a quadratic cost function examining the discrepancy between the observed ($\bar{\eta}_l$) and calculated (η_l) wave surface elevations:

$$F(\mathbf{p}) = \frac{1}{2}\sum_{l=1}^{L} [\eta_l(\mathbf{p}) - \bar{\eta}_l]^2 = \frac{1}{2}\sum_{j=1}^{J}\sum_{k=1}^{K} [\eta_{(j,k)}(\mathbf{p}) - \bar{\eta}_{(j,k)}]^2 \tag{10}$$

where $\mathbf{p} = [a_1, \dots, a_N, b_1, \dots, b_N]^T$ is the model coefficient vector to be obtained, and subscript l denotes the lth spatio-temporal measurement point, which is defined as a pair of $l = (j, k)$; j and k refer to the measured data at the spatial point $r_j = (x_j, y_j)$ and the time t_k, respectively. The total number of spatio-temporal data points L is given by the amount of data in space J at each time and the number of measured points in time K (i.e., $L = J{\times}K$). Next, the derivatives of the cost function with respect to the parameters yield the system of equations with matrix operation $\mathbf{Ap} = \mathbf{B}$:

$$\begin{gathered}\frac{\partial F}{\partial a_m} = 0 \Rightarrow \sum_{l=1}^{L} \eta_l \frac{\partial \eta_l}{\partial a_m} = \sum_{l=1}^{L} \bar{\eta}_l \frac{\partial \eta_l}{\partial a_m} \Rightarrow A_{(m,n)}p_n = B_m \\ \frac{\partial F}{\partial b_m} = 0 \Rightarrow \sum_{l=1}^{L} \eta_l \frac{\partial \eta_l}{\partial b_m} = \sum_{l=1}^{L} \bar{\eta}_l \frac{\partial \eta_l}{\partial b_m} \Rightarrow A_{(N+m,n)}p_n = B_{N+m}\end{gathered} \tag{11}$$

where $n, m \in \{1, \dots, N\}^2$, and it is notable that the greater size of data sets L in this assimilation process leads to a more accurate forecast based on the initial wave coefficients since the optimal initial conditions are determined by an optimization process rather than by the standard Fourier transform method.

2.2.1. Linear assimilation

The assimilation process is dependent on the wave propagation model and we here detail the linear assimilation method specifying the optimal parameters from wave observations:

$$\begin{gathered}A^{LWT}_{(m,n)} = \sum_{l=1}^{L} \cos \psi_{nl} P^{LWT}_{ml}, A^{LWT}_{(m,N+n)} = \sum_{l=1}^{L} \sin \psi_{nl} P^{LWT}_{ml} \\ A^{LWT}_{(N+m,n)} = \sum_{l=1}^{L} \cos \psi_{nl} Q^{LWT}_{ml}, A^{LWT}_{(N+m,N+n)} = \sum_{l=1}^{L} \sin \psi_{nl} Q^{LWT}_{ml} \\ B^{LWT}_{m} = \sum_{l=1}^{L} \bar{\eta}_l P^{LWT}_{ml}, B^{LWT}_{N+m} = \sum_{l=1}^{L} \bar{\eta}_l Q^{LWT}_{ml}\end{gathered} \tag{12}$$

with

$$P^{LWT}_{ml} = \cos \psi_{ml}, Q^{LWT}_{ml} = \sin \psi_{ml} \tag{13}$$

where $\psi_{ml} = \mathbf{k}_{ml} \cdot \mathbf{r}_l - \omega_m t_l$.

2.2.2. Previous nonlinear assimilation

Desmars et al. (2020) derived the nonlinear assimilation problem to determine estimates of wave amplitude parameters in ICWM from wave measurements:

$$A^{ICWM}_{(m,n)} = \sum_{l=1}^{L} (\cos \Psi_{nl} + \frac{1}{2} a_n k_n) P^{ICWM}_{ml}$$

$$A^{ICWM}_{(m,N+n)} = \sum_{l=1}^{L} (\sin \Psi_{nl} + \frac{1}{2} b_n k_n) P^{ICWM}_{ml}$$

$$A^{ICWM}_{(N+m,n)} = \sum_{l=1}^{L} (\cos \Psi_{nl} + \frac{1}{2} a_n k_n) Q^{ICWM}_{ml}$$

$$
\begin{aligned}
A_{(N+m,N+n)}^{ICWM} &= \sum_{l=1}^{L} (\sin \Psi_{nl} + \frac{1}{2} b_n k_n) Q_{ml}^{ICWM} \\
B_m^{ICWM} &= \sum_{l=1}^{L} \bar{\eta}_l P_{ml}^{ICWM}, B_{N+m}^{ICWM} = \sum_{l=1}^{L} \bar{\eta}_l Q_{ml}^{ICWM}
\end{aligned}
\tag{14}
$$

with

$$
\begin{aligned}
P_{ml}^{ICWM} &= \cos \Psi_{ml} - [k_m (a_m \sin \Psi_{ml} - b_m \cos \Psi_{ml}) \\
&\quad \times \{\sin \tilde{\psi}_{ml} - [k_m (a_m \cos \tilde{\psi}_{ml} + b_m \sin \tilde{\psi}_{ml}) + 1] \\
&\quad \times a_m \omega_m k_m t_l\}] + a_m k_m \\
Q_{ml}^{ICWM} &= \sin \Psi_{ml} - [k_m (a_m \sin \Psi_{ml} - b_m \cos \Psi_{ml}) \\
&\quad \times \{-\cos \tilde{\psi}_{ml} - [k_m (a_m \cos \tilde{\psi}_{ml} + b_m \sin \tilde{\psi}_{ml}) + 1] \\
&\quad \times b_m \omega_m k_m t_l\}] + b_m k_m
\end{aligned}
\tag{15}
$$

where $\Psi_{ml} = \mathbf{k}_{ml} \cdot [\mathbf{r}_l - \sum_{i=1}^{N} (-a_i \sin \tilde{\psi}_{il} + b_i \cos \tilde{\psi}_{il})] - \tilde{\omega}_m t_l$ and $\tilde{\psi}_{il} = \mathbf{k}_i \cdot \mathbf{r}_l - \tilde{\omega}_i t_l$. Here, because the nonlinear phase function and thus **A** and **B** include the amplitude parameters, an iterative process is necessary. The solution at the iteration number q can be written $\mathbf{p}^q$. The initial guess for the model parameter vector $\mathbf{p}^0$ is obtained directly from the linear solution and the model parameter vector $\mathbf{p}^{q+1}$ at the current iteration $q + 1$ is obtained based on the wave parameters $\mathbf{p}^q$ at the previous iteration q. The iterations are performed until the relative error between two successive iteration solutions is less than the prescribed tolerance of 10^{-3}. The maximum iteration number is set to 100 to consider the case that converges too slowly and/or diverges.

When we reconstruct the ocean surface over some prespecified domain with frequency and direction cutoffs, especially for multidirectional waves (or short-crested waves), the severely ill-conditioned coefficient matrix **A** could lead to an ill-posed nonlinear assimilation problem. In order to overcome this difficulty, we apply Tikhonov regularization which yields consistent solutions by minimizing the approximated error function:

$$
\min\{\|\mathbf{Ap} - \mathbf{B}\|^2 + r^2 \|\mathbf{p}\|^2\}
\tag{16}
$$

where r is the regularization parameter and $\| \cdot \|$ denotes the Euclidean norm. By employing the "L-curve" method, the regularization parameter is determined (Calvetti et al. 2004, Hansen 2000).

2.2.3. Simplified nonlinear assimilation

As shown in Eqs. (11) through (15), the coefficients matrix **A** is formulated as a multiplication of two factors: the first factor corresponds to the coefficient of a_n or b_n in the equation of wave surface elevation (i.e., η_l), the second factor represents the derivative of the surface elevation with respect to the amplitude parameter (i.e., $P_{ml} = \frac{\partial \eta_l}{\partial a_m}$ or $Q_{ml} = \frac{\partial \eta_l}{\partial b_m}$). The derivation of wave model inversion is given by minimizing the sum of squares of the errors between observations and calculations of each model, therefore, the two factors rely on the wave propagating models (i.e., LWT, LWT-CDR, and ICWM). In comparison to the first factors, the second factors (P and Q) retaining the derivative of the nonlinear phase function with respect to the amplitude coefficients are thus more complicated and sensitive to a_n and b_n. In the present study, in order to gain numerical stability and efficiency in the process of nonlinear assimilation, the nonlinear formulation can be simplified by truncating P and Q up to $O(1)$. The simplified assimilation nonlinear method for ICWM (ICWM-S) is equivalent to that constructed with the first parts of ICWM and the second parts of LWT:

$$
\begin{aligned}
A_{(m,n)}^{ICWM-S} &= \sum_{l=1}^{L} (\cos \Psi_{nl} + \frac{1}{2} a_n k_n) P_{ml}^{LWT} \\
A_{(m,N+n)}^{ICWM-S} &= \sum_{l=1}^{L} (\sin \Psi_{nl} + \frac{1}{2} b_n k_n) P_{ml}^{LWT} \\
A_{(N+m,n)}^{ICWM-S} &= \sum_{l=1}^{L} (\cos \Psi_{nl} + \frac{1}{2} a_n k_n) Q_{ml}^{LWT} \\
A_{(N+m,N+n)}^{ICWM-S} &= \sum_{l=1}^{L} (\sin \Psi_{nl} + \frac{1}{2} b_n k_n) Q_{ml}^{LWT} \\
B_m^{ICWM-S} &= \sum_{l=1}^{L} \bar{\eta}_l P_{ml}^{LWT}, B_{N+m}^{ICWM-S} = \sum_{l=1}^{L} \bar{\eta}_l Q_{ml}^{LWT}
\end{aligned}
\tag{17}
$$

This simplification can be justified on the grounds that the wave steepness is sufficiently small ($ak, bk \ll 1$). As mentioned above, the iterative process is required to find the estimates of wave amplitude parameters in ICWM, which was with the maximum iteration number of 100 as well as an error tolerance of 10^{-3}. This modified assimilation approach would likely enhance nonlinear model stability while maintaining model accuracy if it could reduce the number of iterations required for numerical convergence while achieving consistent results. Hence, this approach is likely to allow for real-time use, especially for multidirectional cases where nonlinear models become far more numerically challenging. We also developed a simplified model inversion for LWT-CDR since the coefficient matrix **A** for LWT-CDR also involves the amplitude coefficients and thus iterations are required. The previous and simplified formulations for LWT-CDR are provided in Appendix.

3. Experimental data

The experimental data were obtained during one of the campaigns of the FLOATECH project conducted in the hydrodynamic and ocean engineering tank at École Centrale de Nantes (ECN) (Bonnefoy et al., 2023). The tank is a 30-m wide, 50-m long, and 5-m deep water testing volume. Irregular sea states were generated using a Pierson–Moskowitz spectrum (Pierson and Moskowitz, 1964) with a peak period $T_p = 12$ s and a significant wave height $H_s = 7$ m at full scale. The test was performed at the geometric scale of 1:40 (1: $\sqrt{40}$ Froude scaling for time). This wave field corresponds to moderate nonlinear waves ($H_s/L_p = 3.1\%$) in deep water ($k_p d \approx 5.6$), with a peak wavelength $L_p = 225$ m (5.62 m in tank scale). Unidirectional and multidirectional waves are generated by a wavemaker at one end of the tank, composed of 48 individual hinged flaps, and absorbed by a 7-m long passive stainless steel beach at the other end.

In order to investigate the effects of directional spreading on the performances of wave models for multidirectional wave fields toward the location of a floating wind turbine, three sea states with a different directional spreading factor s were selected as shown in Table 1 and Fig. 1. For completeness, we also considered a unidirectional case with the same values of H_s and T_p where $s = \infty$ denotes the long-crested waves in Table 1. Wave directionality is taken into account with a complex angular spreading function proposed by Mitsuyasu et al. (1975):

$$
G(\theta) = \frac{2^{2s-1}}{180} \frac{(s!)^2}{(2s)!} \cos^{2s}\left(\frac{\theta}{2}\right) \text{ for } \theta \in [-180°, 180°]
\tag{18}
$$

where the average direction of propagation is 0°. The analysis of the measured wave elevation starts at around $t_a/T_p = 158$, the time at which we consider that all the wave components generated by the wavemaker have reached the end of the wave measurement zone and have evolved in a sufficiently long period of time by nonlinear effects. The wave elevation was recorded until the wavemaker was stopped; therefore, the end of the time series measured in experiments is that used for the prediction study $t_b/T_p \approx 664$, with $t_b - t_a \approx 506 T_p$.

Fig. 2 presents a synthetic optical remote sensing system mounted on an offshore structure model at a location of $(x_c, y_c, z_c) = (19.86 \text{ m}, 15 \text{ m}, 30 \text{ m})$ and the distribution of the wave measurements. This network of wave measurements has been chosen to have a prediction horizon suitable for the control strategies of the wind turbines tested during another experimental campaign, where it should require

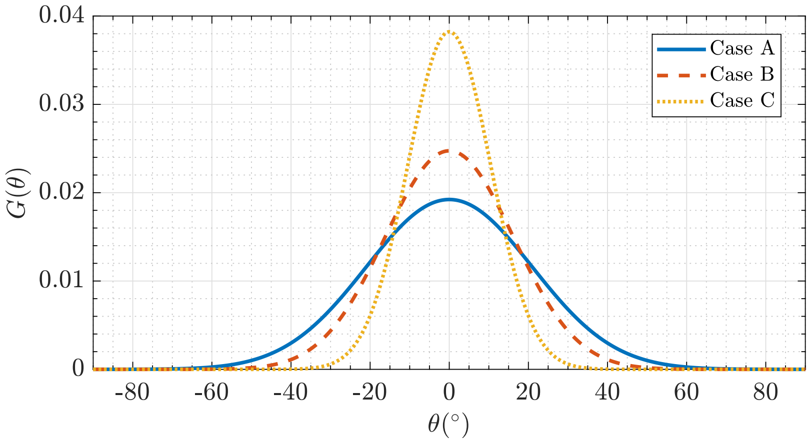

Fig. 1. Directional spreading for multidirectional cases (——: Case A; – – ·: Case B; ⋯⋯: Case C).

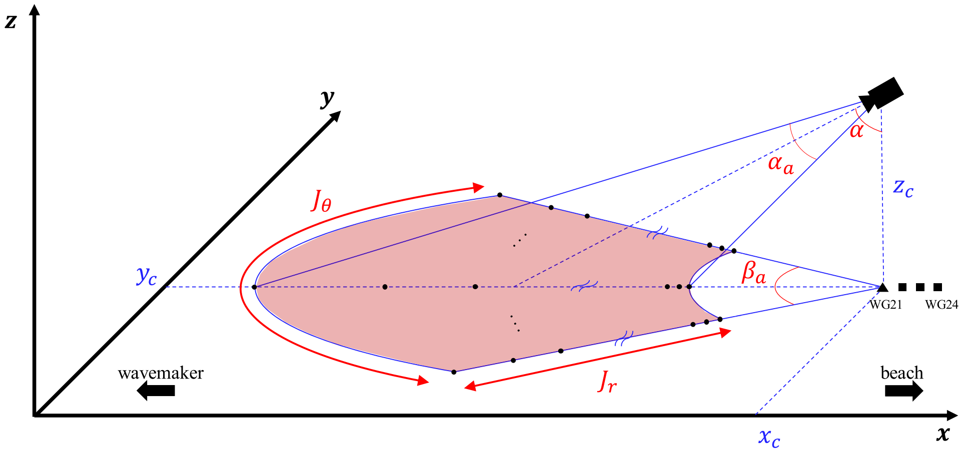

Fig. 2. Spatial sampling of wave field by an optical system (•: wave observations; ▲: location of turbine, WG21; ■: three additional downstream WG22, WG23, and WG24).

Table 1
Directional information of experimental data and numerical simulations.

Case	s	J_θ	N_θ
A	15	11	9
B	25	9	7
C	60	7	5
D	∞	1	1

a relatively short time horizon in wave prediction. Pointing at some distance ($\alpha = 76^\circ$) with vertical and horizontal aperture angles ($\alpha_a = 20^\circ$ and $\beta_a = 48^\circ$ to 76°) and using a matrix of $J_r \times J_\theta$ rays with $J_r = 20$ beams perpendicular to the x-axis at $y = y_c$, measurement points are thus configured in the shape of a radial segment (red shading in Fig. 2). In this experiment, the actual variations in probe location that would be induced by the actual intersection of an optical ray with an irregular evolving free surface were neglected.

The 20 wave gauges installed on a straight structure are allowed to rotate with the following angles in the xy-plane: $\{-38^\circ, -32^\circ, -24^\circ, -16^\circ, -8^\circ, 0^\circ, 8^\circ, 16^\circ, 24^\circ, 32^\circ, 38^\circ\}$ where 0° corresponds to the structure parallel to the x-axis. The sea state had to be repeated several times to make the measurements with different positions of this structure carrying the wave gauges. A total of 47 realizations of the same wave field was performed to assess the repeatability of the experiments; the significant wave height has been estimated for each realization and we found a variation of 6 mm at tank scale (0.24 m at full scale), which indicates the setup shows satisfactory repeatability. By using the rotating structure, we repeated J_θ times with the different angles so that it was possible to construct the network of wave gauges depicted in Fig. 3(a) which mimics the observations by an optical sensor with a horizontal aperture angle.

The spacing between the wave gauges varies with the distance from the center of rotation in order to replicate the distance between beam optical measurements, at varying distances from a remote sensor mounted on the turbine (as shown in Fig. 3). The range of the angular positions of the wave gauges was chosen depending on the directional spreading such that Case A with the greatest spreading used all the range of positions while in Case C, with the smallest directionality, the wave surface elevations were recorded along the range from -24° to 24°. The data of water surface variations were recorded at four additional downstream wave gauges, including the location of the wind turbine (referred to as WG21) and WG24 for the gauge $0.12L_p$ far away from WG21.

4. Prediction zone

4.1. Cutoff frequencies and directions

In order to provide the spatio-temporal prediction zone in which the process of reconstruction and prediction of the phase-resolved wave field is valid, we here prescribe the wave field in terms of frequency and direction, namely, frequency and direction bandwidths. Following the method in Desmars et al. (2020), the upper and lower cutoff limits in frequencies are set by using a small fraction $\mu = 0.05$ of the spectral energy density at peak frequency:

$$S_\eta(\omega_{\min}) = S_\eta(\omega_{\max}) = \mu S_\eta(\omega_p) \qquad (19)$$

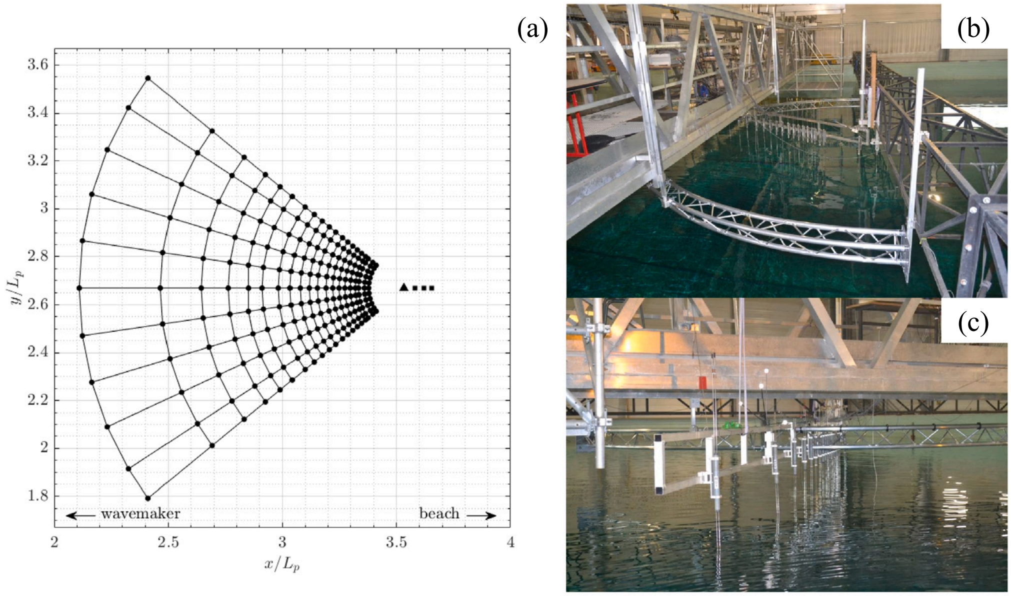

Fig. 3. (a) Location of wave gauges; (b, c) wave gauges mounted on rotating structure (•: wave observations; ▲: location of turbine, WG21; ■: three additional downstream WG22, WG23, and WG24).

where $S_\eta(\omega)$ denotes the wave spectrum at the angular frequency ω and the group velocities $c_{g,\max}$ and $c_{g,\min}$ are related to $\omega_{\min}$ and $\omega_{\max}$ by the deep water approximation of the linear dispersion relation, respectively (i.e., $c_{g,\max} = g/2\omega_{\min}$ and $c_{g,\min} = g/2\omega_{\max}$). Further, the directional cutoff limits $[\theta_{\min}, \theta_{\max}]$ are determined as $\theta_{\min} = -45°$ and $\theta_{\max} = 45°$ since the direction range retains a significant percentage of the spectral energy for all the cases of the present study (e.g., 97.3% in Case A with the greatest directional spread, $s = 15$).

4.2. Multidirectional prediction zone

We defined the finite frequency and direction bandwidths to develop the spatio-temporal prediction zone in which the analysis of wave kinematics and dynamics can be reconstructed and predicted. In this section, we therefore provide the multidirectional prediction zone for the prescribed wave field on the basis of the multidirectional measurements by an optical system mounted on the offshore structure over an assimilation time T_a. The prediction zone for the currently sampled observations in space and time can be obtained by applying the algorithm of developing the prediction zone for multidirectional waves proposed by Qi et al. (2018b) to the present condition. The unidirectional boundary of the predictable spatio-temporal domain is illustrated by an infinite strip perpendicular to the wave propagation direction θ, and thus the multidirectional prediction zone is given by the intersection of the unidirectional prediction zone over all the wave propagating directions, which is limited to $\theta \in [-45°, 45°]$ in the present study. The direction may have to be restricted within a narrower range in reality since the optical system has a more limited finite range of direction arriving at the floating offshore wind turbines. Further, the prediction zone is governed by the group velocity, which was confirmed by several numerical investigations (Wu 2004, Naaijen et al. 2014) and by mathematical analysis (Qi et al., 2018b). For simplicity, we here assume linearized wave theory in determining the prediction zone. Readers may refer to Qi et al. (2018a) for the nonlinear prediction zone incorporating the second-order nonlinear dispersion effects.

Fig. 4 shows the observation or prediction zone, in which red and gray shadings illustrate the process of nowcast and forecast, respectively. With $J_r{\times}J_\theta$ measurement points shown in Fig. 4(a), the observation area is bounded as a shape of radial segment $ABCDEFGHI$ in Fig. 4(b), where points B to F are measurements located on the left boundary of the observation zone, points I and H are the farthest points from the wavemaker and on the right boundary of the observation zone, point A is the point of intersection between the left boundary of $\theta_{\min} = -45°$ and the right boundary of $\theta_{\max} = 45°$ (i.e., $x = y'+x_B-y'_B$ and $x = -y'+x_I+y'_I$ in Fig. 4(b), respectively), and point G is a reflected point of point A over $y' = 0$ (or $y = y_c$). Due to the small distances in the x-direction between points in the first column, we can approximate the left boundary of the observation and prediction zones by the ones with three measurements B, D, and F. A similar approximation for the right boundary with a single point H can also be made from Fig. 4(c). As in the unidirectional case from Desmars et al. (2020), when the spatio-temporal data sets are considered for an assimilation procedure with an assimilation time T_a, we have the extended prediction zone due to the right boundary of the prediction zone that propagates with the minimum group velocity $c_{g,\min}$ over the assimilation time T_a (see Fig. 4(d)).

4.3. Temporal evolution of the prediction zone

From the latest time of wave reconstruction $t = t_r$ (or by the index for time $k = K$) or when one starts to forecast the wave field by the assimilated wave information, the left boundary propagates with $c_{g,\max}$ or the speed related to $c_{g,\max}$ whereas the right boundary is determined by the values with $c_{g,\min}$. Accordingly, the predictable domain begins to shrink and finally disappears as the left boundary moves ahead of the right boundary.

Fig. 5 illustrates the temporal evolution of the prediction zone over the time duration $t' = t - t_r \in [0, t'_3+]$ (where t'_3+ is when the prediction zone disappears). Since the x-component of the group velocity of θ (i.e., $c_g/\cos\theta$) increases with the propagating direction θ, the lines with the greatest θ that pass through the measurement points (i.e., B, D, and F) determine the left boundary of the prediction zone. Therefore, the prediction zone around point D is bounded by the segments BD and DF propagating with $\frac{c_{g,\max}}{\cos(\theta_B/2)}$, where half of the horizontal aperture angle is $\theta_B = \frac{\beta_a}{2}$. Also, the area outside of points B and F is defined by the lines of $\theta_{min} - 45°$ and $\theta_{max} = 45°$, which propagate fastest in the $+x$-direction and thus the left boundary is eventually determined by these two lines. On the other hand, given the single fixed probes H, the right boundary is given by the intersection of the prediction zone over all the

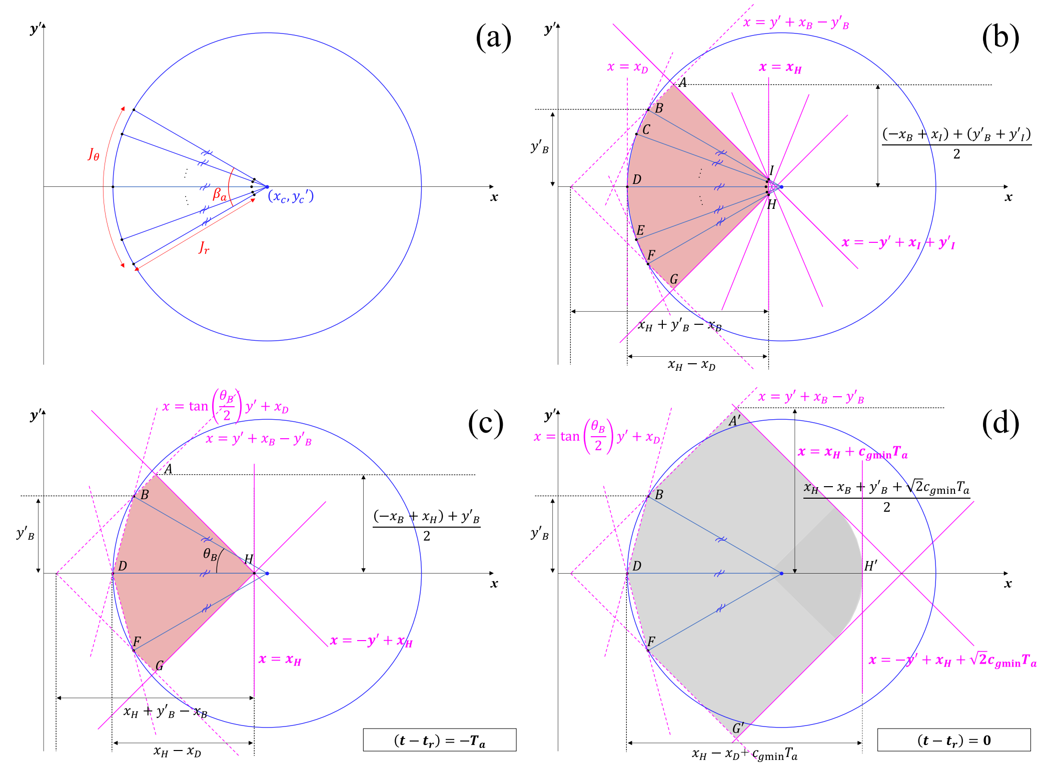

Fig. 4. Observation and prediction zones: (a) measurement points; (b) observation zone; (c) $(t - t_r) = -T_a$; (d) $(t - t_r) = 0$ (- - -: left boundary; ——: right boundary; red shading: nowcast; gray shading: forecast).

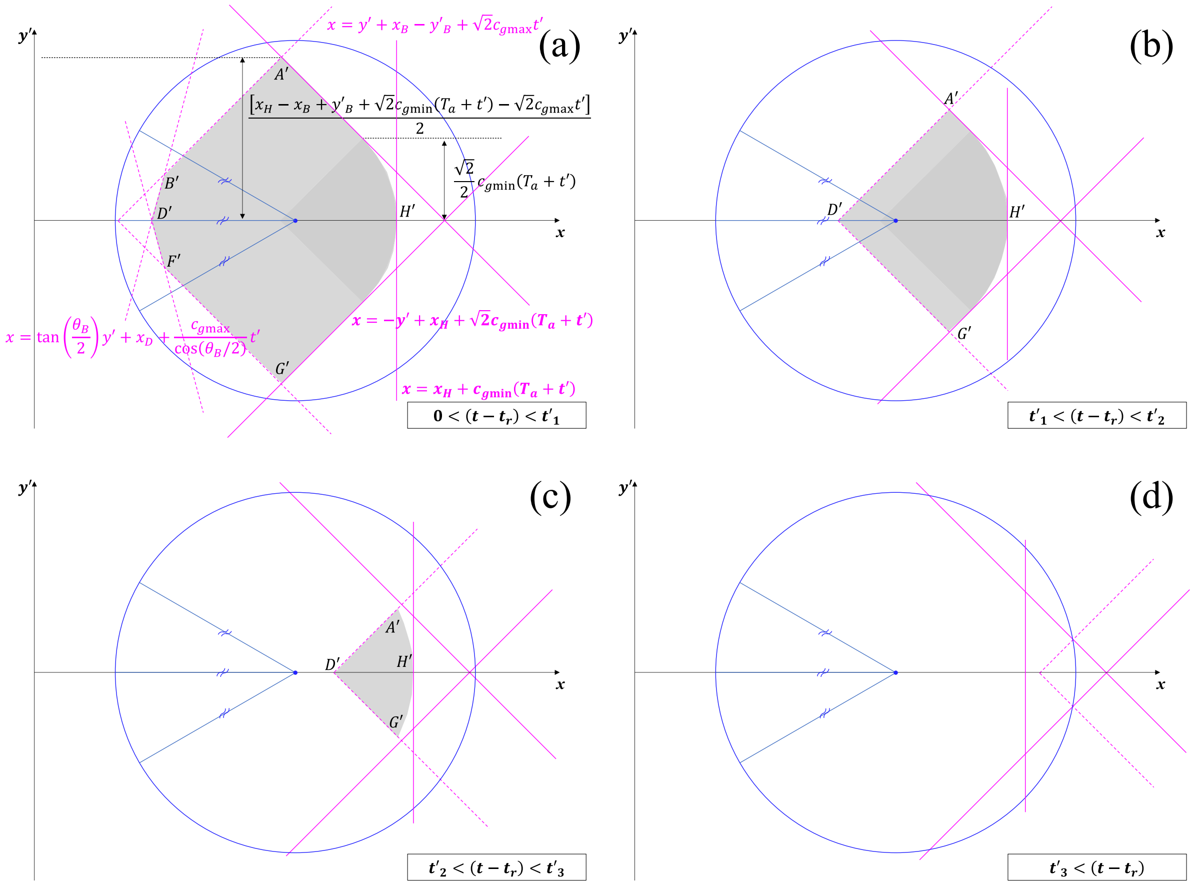

Fig. 5. Temporal evolution of prediction zone: (a) $0 < (t - t_r) < t'_1$; (b) $t'_1 < (t - t_r) < t'_2$; (c) $t'_2 < (t - t_r) < t'_3$; (d) $t'_3 < (t - t_r)$.

wave propagating directions, corresponding to the fan-shaped line (Qi et al., 2018b):

$$\max\begin{bmatrix} y' + x_B - y'_B + \frac{c_{g,\max}}{\cos 45^\circ} t', \\ -y' + x_F + y'_F + \frac{c_{g,\max}}{\cos 45^\circ} t', \\ \pm \tan\frac{\theta_B}{2} y' + x_D + \frac{c_{g,\max}}{\cos(\theta_B/2)} t' \end{bmatrix} \le x \le \min_{\theta\in[-45^\circ,45^\circ]} \begin{bmatrix} -\tan\theta y' + x_H \\ + \frac{c_{g,\min}(T_a+t')}{\cos\theta} \end{bmatrix} \tag{20}$$

where $y' = y - y_c$ and $t' = t - t_r \geq -T_a$. The temporal prediction zone $t' \in [t'_{\min}, t'_{\max}]$ at any location along the centerline $y = y_c$ can be obtained by manipulating Eq. (20) with respect to time:

$$\begin{aligned} t'_{\min} &= \max[-T_a, -T_a + \frac{x - x_H}{c_{g\,\min}}] \\ t'_{\max} &= \min[\frac{x - x_D}{c_{g\,\max}}\cos(\theta_B/2), \frac{x - x_B + y'_B}{c_{g\,\max}}\cos 45^\circ] \end{aligned} \tag{21}$$

which can be reduced to the temporal prediction zone of the unidirectional case by substituting $\theta_B = 0$. In addition, because the segments with the different propagating speeds in the $+x$-direction compose the boundaries of the prediction zone, as time increases, the prediction zone evolves with four different shapes including the last stage with no prediction zone in Fig. 5(d):

$$\begin{aligned} t'_1 &= \frac{x_D + y'_B - x_B}{c_{g\,\max}/\cos 45^\circ - c_{g\,\max}/\cos(\theta_B/2)} \\ t'_2 &= \frac{x_H - x_B + y'_B}{c_{g\,\max}/\cos 45^\circ} \\ t'_3 &= \frac{x_H - x_B + y'_B + c_{g\,\min}T_a}{c_{g\,\max}/\cos 45^\circ - c_{g\,\min}/\cos 45^\circ} \end{aligned} \tag{22}$$

5. Numerical simulations

5.1. Normalized misfit error

In previous studies (Naaijen et al. 2014, Desmars et al. 2020), to accurately evaluate the performance of numerical models, an ensemble average of prediction error was employed by using partly overlapping surface samples, shifted in time by Δt. The size of the time shift of the surface sample Δt is directly related to the total number of surface samples N_s required to yield the convergence. Desmars et al. (2020) showed that a smaller Δt results in faster convergence for the prediction error and thus leads to a reduction in the total time duration during the assimilation procedure over N_s samples (i.e., $T_c = T_a + (N_s - 1)\Delta t$) although the value of the convergence error is independent of Δt. Accordingly, we used $\Delta t/T_p = 0.053$ which is close to the value in Desmars et al. (2020).

The ensemble average of the normalized misfit error is calculated to quantify the model performances over the predictable domain. It ranges from 0 to ∞, with 0 corresponding to the ideal model:

$$\epsilon(x, y, t) = \frac{1}{N_s}\sum_{i=1}^{N_s} \frac{\left|\eta_{pred,i}(x, y, t) - \eta_{ref,i}(x, y, t)\right|}{H_s} \tag{23}$$

where $\eta_{pred,i}$ and $\eta_{ref,i}$ are the predicted and observed surface elevation of the ith surface sample, respectively. In order to assess the overall prediction error over the prediction zone in time at a specific point (x, y), the misfit error is further averaged over the time prediction zone $[t_{\min}, t_{\max}]$:

$$\epsilon^p(x, y) = \frac{1}{t_{\max} - t_{\min}}\int_{t_{\min}}^{t_{\max}} \epsilon(x, y, t)\,dt \tag{24}$$

Fig. 6 illustrates the averaged prediction error between the surface predicted by ICWM and the reference surface against T_c/T_p. Here, $T_a/T_p \approx 5.2$ was used, and the study of the assimilation time T_a will be detailed in the next section. For all the cases, the prediction errors are converged for $T_c/T_p \approx 25$ corresponding to $N_s = 400$. Further, in order to examine the effect of directional spreading on the rate of prediction error convergence, we calculated the coefficients of variance of the misfit error (COV, the ratio of the standard deviation to the mean) over N_s samples. While the value of COV for multidirectional cases was around 10%, the unidirectional case D yielded a COV value of about 17%. These results are expected since the numbers of wave parameters and measurements increase significantly when addressing directional spreading in multidirectional cases. Nevertheless, the convergence of the prediction error with respect to T_c/T_p (or N_s) is quite acceptable for all the cases in this study.

5.2. Parameters of the prediction algorithm

Nouguier et al. (2013) employed a single snapshot of the ocean surface made by a LIDAR camera at grazing incidence in the assimilation procedure and showed that the model prediction from the reconstructed wave field depends on the footprint area size by the optical system. Recently, Desmars et al. (2020) defined the bandwidths of the reconstructed wave field based on the largest gap between two gauges and the distance that the upper boundary travels with the slowest group velocity within the frequency bandwidth c_{g,N_ω} over the assimilation time T_a leading to the extended reconstructed wave field.

The number of measurement points in time K relies on the assimilation time T_a, which is thus strongly related to the model accuracy as well as to numerical cost. As a result of sensitivity analysis with respect to the assimilation time T_a and to provide a good compromise between computational efficiency and numerical accuracy, we use $T_a/T_p \approx 5.2$ (or $K = 100$) which yields the convergence error as shown in Fig. 7. It is notable that the required numbers of peak wave periods for the total time window and the assimilation time (i.e., T_c/T_p and T_a/T_p) yielding the convergence error in the present cases are less than that in the case from Desmars et al. (2020), which were $T_c/T_p \approx 60$ and $T_a/T_p \approx 7$. This is an expected result since the propagating distance from the observation zone to the location of the turbine (i.e., from WG20 to WG21, about $0.15L_p$) was smaller than the condition in Desmars et al. (2020), where the distance was about $0.4L_p$.

From the numerical point of view, we should use the extensive bandwidth which is independently determined from the one for the prediction zone (Eq. (19)). This is because the wave information used in the assimilation and prediction procedure directly depends on the distance in the x-direction between the beginning and end of the wave gauges for each case (x_b and x_e) and the advection of wave information during T_a. On the one hand, x_b is set to the same location, the first point in the structure of 0° (WG1) for all the cases because the structure rotating about the location of the turbine provides the measurement zone. On the other hand, x_e varies depending on the case due to the decreasing distance in the x-direction between WG21 and the last point of the structure with rotating angles. Thus, we have the greatest distance between x_b and x_e in Case A including all the angles from −38° to 38° in the observations of ocean surface despite the minor differences between cases. The minimum wavenumber k_1 is then given by:

$$k_1 = \frac{2\pi}{x_e - x_b + c_{g,N_\omega}T_a} \tag{25}$$

where the slowest group velocity c_{g,N_ω} corresponds to the group velocity of the N_ωth wave component ($c_{g,N_\omega} = \frac{1}{2}\sqrt{g/k_{N_\omega}}$). Therefore, it is necessary to specify the last frequency component's wavenumber k_{N_ω} in advance above which the description of the wave field is negligible and can thus be discarded. In the previous study (Desmars et al., 2020), $k_{N_\omega} = 20k_p$ with $N_\omega = 50$ was used, which satisfies the Nyquist–Shannon sampling theorem $20k_p < \min_{\Delta x} \frac{2\pi}{2\Delta x}$. In order to achieve a good balance between computational cost and model accuracy, we conducted the sensitivity analysis with respect to k_{N_ω}, which is omitted here for brevity. As a result, we use $k_{N_\omega} = 12k_p$ with $N_\omega = 30$, which maintains practically the same accuracy (i.e., at WG21) but requires

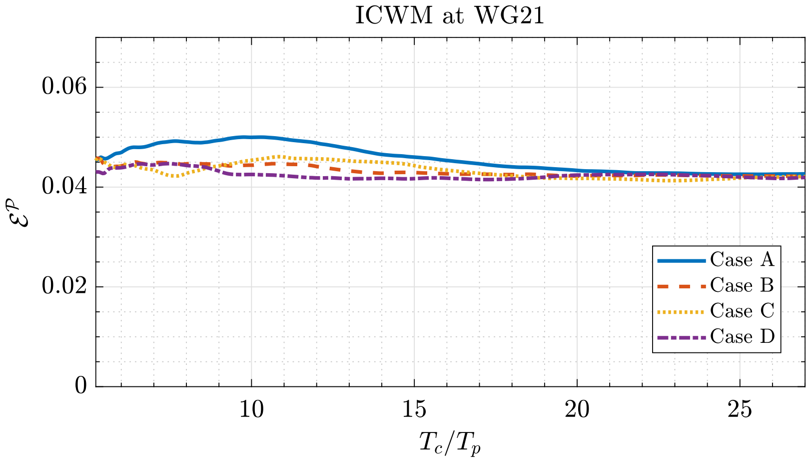

Fig. 6. Prediction error of ICWM at WG21 against T_c/T_p (——: Case A; – – ·: Case B; ······: Case C; —·—: Case D).

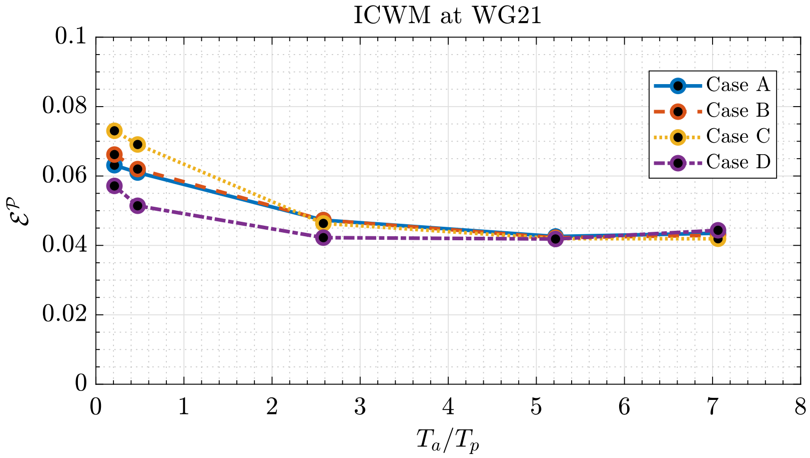

Fig. 7. Prediction error of ICWM at WG21 against T_a/T_p (——: Case A; – – ·: Case B; ······: Case C; —·—: Case D).

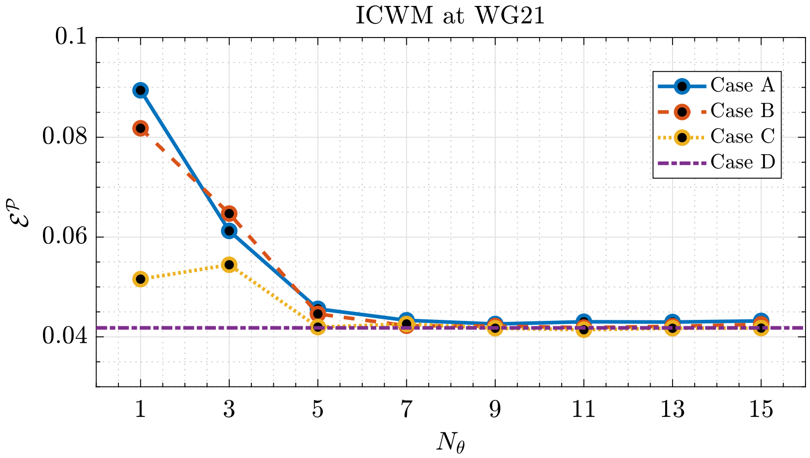

Fig. 8. Prediction error of ICWM at WG21 against N_θ (——: Case A; – – ·: Case B; ······: Case C; —·—: Case D).

significantly less computational effort (about 30%) compared to $k_{N_\omega} = 20k_p$ with $N_\omega = 50$ for all the directional cases.

We note that the same directional cutoff limits as for the prediction zone $[\theta_{\min} = -45°, \theta_{\max} = 45°]$ are used to describe the ocean surface as well. To optimize the number of directional components N_θ, we also studied the convergence of the averaged prediction error at WG21 in the temporal prediction zone. Fig. 8 shows the results of sensitivity analysis with respect to the optimal size of wave component in direction for each case yielding the converged error (see Table 1). The dash–dot line indicates the converged error for the unidirectional case D as a reference error. As expected, the greater N_θ gives a smaller error, particularly in comparison with the unidirectional approach ($N_\theta = 1$), since the multidirectional approach reduces the misfit error ε^p significantly. Two features are apparent with increasing directional spreading:

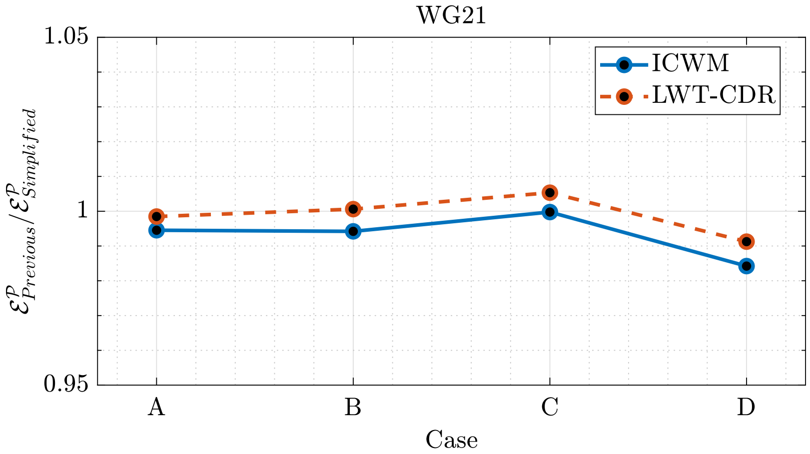

Fig. 9. Comparison of prediction error between the previous assimilation from Desmars et al. (2020) and the simplified assimilation at WG21 (——: ICWM; – – ·: LWT-CDR).

(1) a larger reduction in the prediction error for the directional cases thanks to the consideration of the directional component compared to the unidirectional approach with $N_\theta = 1$; (2) an increase in the optimized number of N_θ (despite minor differences between using N_θ larger or equal to 5 for each case). The determined values of N_θ meet the condition for the unique solution in reconstruction for all the cases ($N_\theta < J = J_r \times J_\theta$, Qi et al. 2018a). Owing to the small number of directional components N_θ, we use a linear distribution of the wavenumbers in direction, while a logarithmically spaced wavenumber in frequency is used to allow a better focus on the part of the spectrum around the peak wavenumber.

5.3. Effect of simplified assimilation

In addition to the wave frequency component, the directional component is considered to reconstruct the initial wave conditions for multidirectional waves from the two-dimensional wave measurements on the xy-plane. Since the numbers of wave components and measurements are multiplied by a factor of N_θ and J_θ compared to the unidirectional case, respectively, the computation time increases significantly during the real-time wave prediction. Thus, as the numbers of wave components and observation points increase with the directional spreading, real-time wave prediction becomes more prohibitive, in particular for the advanced nonlinear model (i.e., ICWM). To overcome this real-time constraint, we developed a simplified nonlinear assimilation for ICWM and LWT-CDR (see Section 2.2.3 and Appendix, respectively) by simplifying part of the coefficients matrix **A**. In this section, in order to justify the simplified approach for nonlinear assimilation, we investigate the effect of the simplified assimilation in terms of computational efficiency and stability as well as model accuracy.

The real-time system generally has a total numerical time T_{total}, composed of times for nowcast $T_{nowcast}$ and forecasts $T_{forecast}$, which must be smaller than the length of the practical prediction zone in time at the location of the turbine (i.e., $T_{total} < t'_{\max} = t_{\max} - t_r$, see Eq. (21)). The length of the practical prediction zone from the latest time of nowcast t_r until WG21 falls outside the prediction zone $t_{\max}$ is about $1.8T_p = 21.6$ s at full scale. Fig. 9 compares the averaged prediction error by both assimilation methods for each model at WG21. All the computations were run on an Intel(R) Core(TM) i7-8700 CPU 3.20 GHz. Table 2 compares the numerical efficiency (time duration) and stability (iteration number and convergence probability) between the previous assimilation from Desmars et al. (2020) (hereinafter Previous in figures and tables) and the present assimilation (hereinafter Simplified in figures and tables) of each wave model for one surface sample in Case A, the most demanding case for real-time prediction with the greatest J_θ and N_θ.

Table 2
Comparison of numerical cost and stability between the assimilation methods for Case A at WG21 where the practical prediction zone in time $t_{\max} - t_r \approx 21.6$ s at full scale.

Model	LWT	ICWM		LWT-CDR	
		Previous	Simplified	Previous	Simplified
$T_{nowcast}$ (s)	1.1	95.7	7.6	52.1	3.0
$T_{forecast}$ (s)	< 0.01	< 0.01	< 0.01	< 0.01	< 0.01
T_{total} (s)	1.7	95.7	7.6	52.1	3.0
Iteration number (max = 100)	–	22.7	5.8	15.9	3.0
Convergence probability ($N_s = 400$)	–	83.5% (334)	98.5% (394)	88% (352)	100% (400)

It is confirmed that the time duration for the forecast appears to be negligible in comparison to the time duration for the nowcast as well as the practical time prediction zone. As expected, the most mature models with more nonlinearity (i.e., ICWM) and the previous assimilation are computationally more expensive and unstable than other wave models and simplified ones, respectively. In addition, compared to the previous assimilation, the simplified method provides almost the same results for both ICWM and LWT-CDR as shown in Fig. 9. It is notable that the difference between the two assimilation methods is negligible with respect to the initial errors. Therefore, the simplified one is even more advantageous for the real-time system of these multidirectional cases with greater spreading. More specifically, with the previous assimilation, LWT-CDR cannot satisfy the real-time constraints, while the simplified one renders not only LWT-CDR but also ICWM to accomplish the real-time prediction in time.

6. Results

6.1. Evolution of surface elevation and prediction error

Fig. 10 compares the time evolution of wave surface elevation at the location of the turbine (i.e., WG21) by all the models including LWT, LWT-CDR, and ICWM to that of experimental reference data for all the cases in Table 1. All the model predictions match well with the experimental data regardless of the directional spreading and whether the case is unidirectional or multidirectional. However, the predictions of all the models demonstrate minor but consistent deviations from the measured surface elevation. One likely reason for the deviations involves experimental noise: By comparing the experimental and numerical surface elevation data to the simulated results in the equivalent experimental setup, but with a somewhat shorter peak period ($T_p = 10$

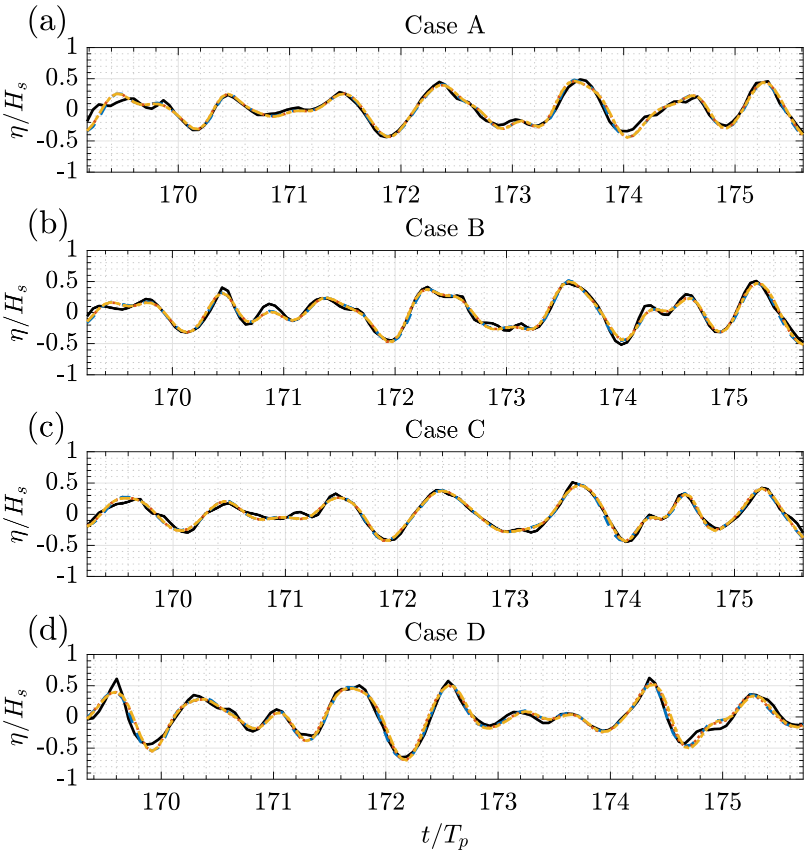

Fig. 10. Time series of surface elevation at WG21: (a) Case A; (b) Case B; (c) Case C; (d) Case D (——: Data; – – ·: ICWM; ⋯⋯: LWT-CDR; —·—: LWT).

s), Desmars et al. (2020) confirmed that experimental noise causes the relatively constant prediction error regardless of the wave models. Despite the fact that the effect of nonlinearity by ICWM is not visually apparent, we will demonstrate in the following sections that the nonlinear model not only achieves better accuracy in describing the ocean wave surface but also grasps the essential properties in the evolution of the wave spectrum with various quantities such as cross-correlation, wave spectral density as well as the estimate of surface shape.

Fig. 11(a) shows the evolution of the ensemble average of the normalized misfit error ε at WG21 for Case B, in which directional spreading of the wave is intermediate among all the directional cases in the present study. Two-dimensional spatio-temporal evolution of the prediction error along the centerline at $y = y_c$ (see Fig. 2) and three-dimensional spatio-temporal evolution of the prediction error over the entire domain in the xy-plane are illustrated in Figs. 11(b) and 12, respectively. As shown in Fig. 11, the prediction zone denoted by two black dash–dot lines (Eq. (21)) coincides with the area where the prediction errors decrease significantly decreased. The value of minimum error is 3.67% by ICWM, while it is 3.99% by LWT and 3.81% by LWT-CDR, i.e. about 4% and 9% larger compared to ICWM, respectively. One can observe at both boundaries of the prediction zone that the error rises steeply toward the outside of the prediction zone because the wave field which is *a priori* analyzed and to be predicted has not yet arrived or has already passed through WG21. Consequently, ICWM is in a relatively more advantageous position at the upper boundary of the time prediction zone $t = t_{\max}$ with the maximum misfit error of 5.93%, while it is 6.74% by LWT and 6.17% by LWT-CDR, i.e. about 4% and 14% larger compared to ICWM, respectively.

From both two- and three-dimensional spatio-temporal visualizations for the evolution of the prediction error, the spatio-temporal data sets for the assimilation procedure with assimilation time T_a yield an extension to the prediction zone: (1) the observation zone at $(t-t_r)/T_p = -T_a/T_p$ explains the spatial prediction zone when only the data in space are used, namely, the bottom line of the black rectangle in Fig. 11(b) which is a horizontal projection of the red shading in Fig. 12(a); (2) the extended prediction zone is encompassed by two dash–dot lines at $(t - t_r)/T_p = 0$ in Fig. 11(b), corresponding to the gray shading in Fig. 12(b). Note that the right boundary of the spatial prediction zone is not shown here in Figs. 11(b) and 12(b) since it is beyond the axis limit. As illustrated with the filled circles at the location of WGs including the additional downstream WGs in Fig. 12, the two-dimensional prediction zone in the xy-plane is valid where the prediction error is consistently low within the prediction zone in the same manner as Fig. 11.

6.2. Comparison between wave models

In wave scattering modeling from sea surfaces for remote sensing, the free surface slope plays an important role in providing a realistic description of the ocean sea surface, especially in the more severe sea state which can no longer remain Gaussian throughout the wave evolution and where nonlinearity thus becomes more necessary (e.g., Nouguier et al. 2010, 2013). Owing to the small distance ($\approx 0.02L_p$) between the last two wave observations along $y = y_c$ used in the assimilation (referred to as WG19 and WG20), a gradient of wave surface elevation between WG19 and WG20 gives an estimate of the surface slope $ss(t)$:

$$ss(t) = \frac{\eta(x_{20}, y_c, t) - \eta(x_{19}, y_c, t)}{x_{20} - x_{19}} \tag{26}$$

where x_{19} and x_{20} denote the x-coordinates of WG19 and WG20, respectively. Also, in order to separately assess the effects of the nonlinear phase shift (i.e., wave geometry or wave shape) and Stokes drift (i.e., time shift in phase), the maximum cross-correlation and corresponding time-lag are examined, respectively:

$$C(\tau) = \frac{1}{t_{\max} - t_{\min}} \int_{t_{\min}}^{t_{\max}} \hat{\eta}_{pred}(t) \times \hat{\eta}_{ref}(t + \tau) dt \tag{27}$$

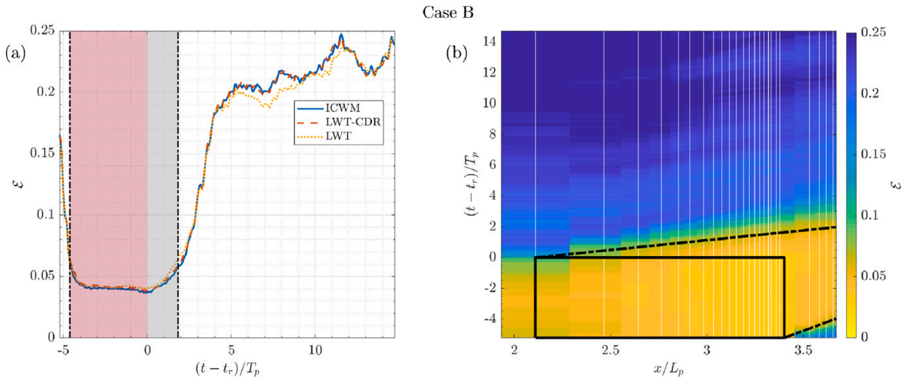

Fig. 11. Evolution of prediction error for Case B: (a) using all models at WG21; (b) using ICWM at all WGs along centerline at $y = y_c$ (——: ICWM; – – ·: LWT-CDR; ······: LWT; —·—: boundaries of prediction zone; red shading: nowcast; gray shading: forecast; vertical white lines: x-location of WGs along centerline at $y = y_c$; black rectangle: assimilated data set).

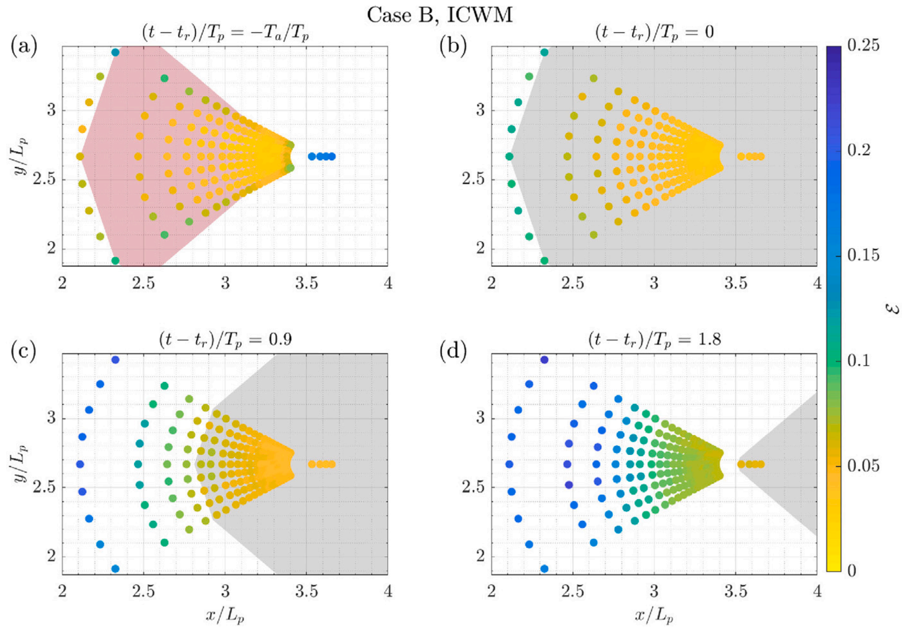

Fig. 12. Spatio-temporal evolution of prediction error for Case B using ICWM: (a) $(t-t_r)/T_p = -T_a/T_p$; (b) $(t-t_r)/T_p = 0$; (c) $(t-t_r)/T_p = 0.9$; (d) $(t-t_r)/T_p = 1.8$ (filled circles: prediction error at WGs; red shading: nowcast; gray shading: forecast).

where the dimensionless free surface elevation $\hat{\eta} = \eta/\sigma_{\eta_{ref}}$ is normalized by the standard deviation of the reference surface for both prediction and reference values. We note that by normalizing the elevations with respect to the reference data, the cross-correlation can provide a measure of the similarity of two series in terms of shape and magnitude, with $\max(C) = 1$ corresponding to the ideal match.

Fig. 13 shows the ratio of prediction error by ICWM to that of LWT-CDR and of LWT not only for the surface elevation but also for the surface slope at WG20. Fig. 14 compares the maximum cross-correlation and corresponding normalized time lag between the numerical wave models at WG21. Error bars are added based on the time resolution of the measurements in Fig. 14(b). For the multidirectional cases, the trend in the prediction misfit error and correlation is very similar for each case, in other words, the directional spreading is not likely to affect the performances of wave models for multidirectional wave fields. This may be due, even in Case A with the greatest spreading of the directional cases in this study, to the fact that the spectral energy is fairly well concentrated around the mean propagating direction (i.e., 0°) and the angular spreading is so moderate that most of the energy is contained in the not-wide angle range of $[-45°, 45°]$. It coincides with the finding that there is little difference not only in the converged prediction error between the directional cases but also in the results between using N_θ larger or equal to 5 for each case in optimizing the number of directional wave components (see Fig. 8).

As shown in Fig. 13, the relative errors of ICWM for the surface elevation compared to LWT as well as LWT-CDR are greater than about 96% in the multidirectional cases, while only LWT exhibits a relatively strong deviation from the reference data for the surface elevation in the unidirectional case D. This implies that, if the wave field is directionally spread, the effect of Stokes drift, which is not included in LWT, becomes negligible in comparison to the unidirectional case. Since the nonlinearity of Stokes drift is at third order in wave steepness (or second order in the expression of elevation), the summation of the directional wave components becomes less dominant than that in the unidirectional condition, the larger the wave steepness. This fact can explain the results in Fig. 14(b) showing that the time-lags of all the models are close to zero and have overlapping error bars for all the cases whereas the time-lag of LWT is about a few percent of the peak period in Case D.

Unlike the effect of Stokes drift in the wave celerity, the nonlinear phase shift (i.e., summation in Eq. (6)) is expected to be similarly crucial whether or not the wave field spreads directionally because the

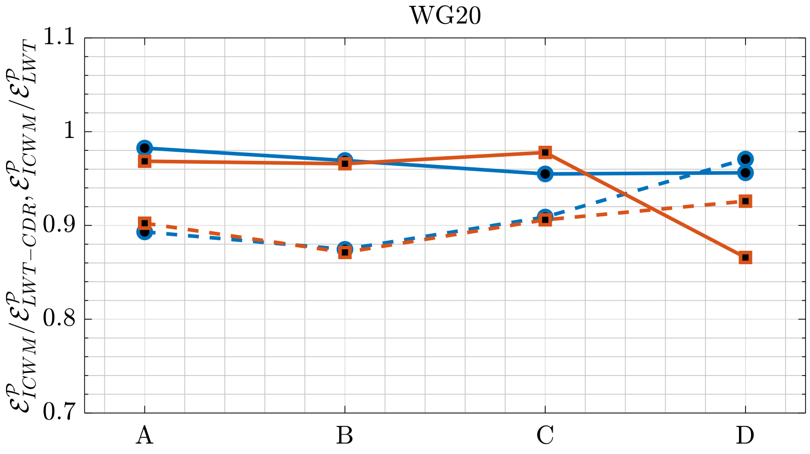

Fig. 13. Comparison of prediction error between ICWM and LWT-CDR (•); ICWM and LWT (■) at WG20 (——: surface elevation η; – – -: surface slope ss).

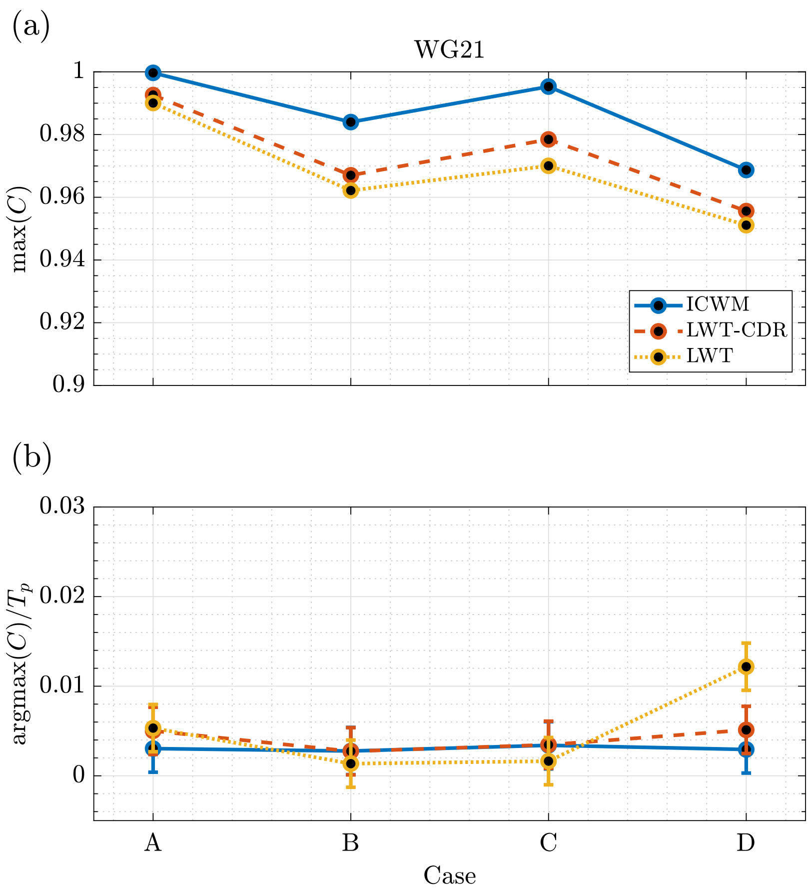

Fig. 14. Cross-correlation between predicted and measured surface elevations at WG21: (a) maximum value; (b) corresponding normalized time-lag (——: ICWM; – – -: LWT-CDR; ⋯⋯: LWT).

geometrical correction in the celerity of ICWM is at second order in wave steepness (or first order in the expression of elevation). It is found from the ratio of ICWM to LWT-CDR and LWT for the ss prediction error which reaches approximately 0.9 in Fig. 13 and the relatively constant improvement by ICWM for max(C) compared to the other models for all the cases in Fig. 14(a). The only exception is observed between ICWM and LWT-CDR prediction errors of the surface slope for Case D shown in Fig. 13. This can probably be attributed to the experimental noise resulting from perturbations by the wavemaker.

In order to investigate how the model performances change as waves propagate in space (or downstream), we compared the results of ICWM for the maximum cross-correlation, corresponding time lag, and prediction error at WG21, 22, 23, and 24 (for which the propagating distances from WG20 are $0.15L_p$, $0.21L_p$, $0.24L_p$, and $0.28L_p$, respectively, see Fig. 15). Except for the time lag where the error bars overlap, the comparison of the model results at the downstream wave gauges shows that as the waves propagate in space, the deviation of the nonlinear model from the data becomes more pronounced. This is consistent with the finding of Desmars et al. (2020) that the maximum cross-correlation tends to decrease with the increasing distance downstream when the steepness exceeds 2.5% (H_s/L_p = 3.11% here). Note that due to the normalized model prediction by the reference

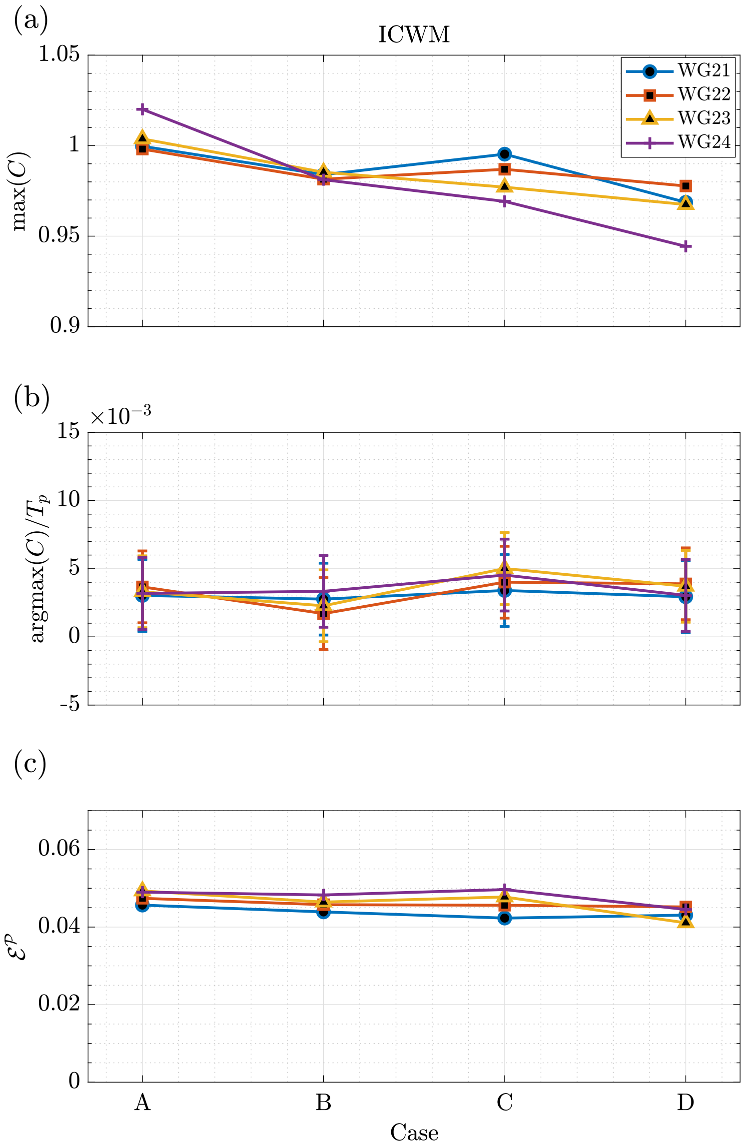

Fig. 15. Spatial evolution of model performances by ICWM along downstream WGs: (a) maximum cross-correlation; (b) corresponding normalized time-lag; (c) prediction error for surface elevation (•: WG21; ■: WG22; ▲: WG23; +: WG24).

data, the maximum cross-correlation above unity ($\max(C) > 1$) indicates overprediction, namely, deviation from the reference data. This is expected as we chose a less strict frequency range to explain the prediction zone, the reconstructed wave components are increasingly limited to achieving the physical representation of the wave field as the location moves farther from the observation zone.

6.3. Continuous wave prediction

To have a reliable estimate of the wave spectrum, we extracted the wave spectrum from the continuous time series of surface elevation for the whole experimental duration up to t_b (where $t_b/T_p \approx 664$). Fig. 16 depicts the evolution of the normalized spectral energy density of the free surface elevation $S_\eta^* = S_\eta f_p/(H_s^2/16)$ obtained by the time series at WG21 for Cases B and D. Overall, comparing the model results to the experimental data in both unidirectional and multidirectional cases, two features are apparent: (1) every model works reasonably well for the lower frequency range waves shown in Fig. 16(a) and (c); (2) ICWM exhibits a significant improvement in resolving the higher frequencies shown in Fig. 16(b) and (d). The advantage of ICWM for the higher frequency range can be explained by the fact that ICWM accounts for the bound waves as a result of including the nonlinear phase shift in the nonlinear phase function (i.e., Ψ), which is directly related to the better performance by ICWM for the measures pertaining to the wave shape such as surface slope predictions and maximum cross-correlation value. In addition, the generation of wave energy over the higher wave energy where the energy is not initially assigned ($f/f_p > 3.46$ or $k/k_p > 12$) is a typical manifestation of bound waves by ICWM.

In order to quantitatively evaluate the accuracy of the sea surface prediction, the surface similarity parameter (SSP), which is zero for an ideal wave model, was proposed by Perlin and Bustamante (2016). In this study, we used an improved surface similarity parameter (ISSP) for the surface elevation with reference to Willmott (1982) to include the deviation of the predicted value from the averaged reference value:

$$ISSP = \frac{\left(\int \left|F_{\eta,pred}(f) - F_{\eta,ref}(f)\right|^2 df\right)^{1/2}}{\left(\int \left[\left|F_{\eta,pred}(f) - \overline{F}_{\eta,ref}\right| + \left|F_{\eta,ref}(f) - \overline{F}_{\eta,ref}\right|\right]^2 df\right)^{1/2}} \tag{28}$$

where $F_{\eta,pred}$ and $F_{\eta,pred}$ are Fourier transforms of surface elevation time series for prediction and reference values, respectively. The overbar denotes the averaged value over the entire frequency range.

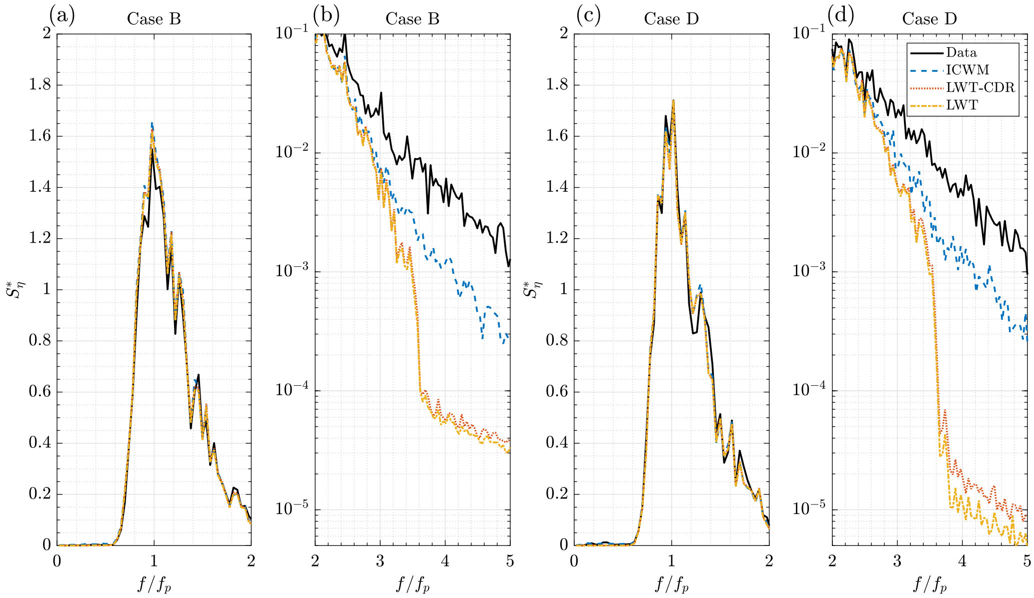

Fig. 16. Normalized wave spectra of surface elevation at WG21: (a, b) Case B; (c, d) Case D (——: Data; – – -: ICWM; ⋯⋯: LWT-CDR; —·—: LWT).

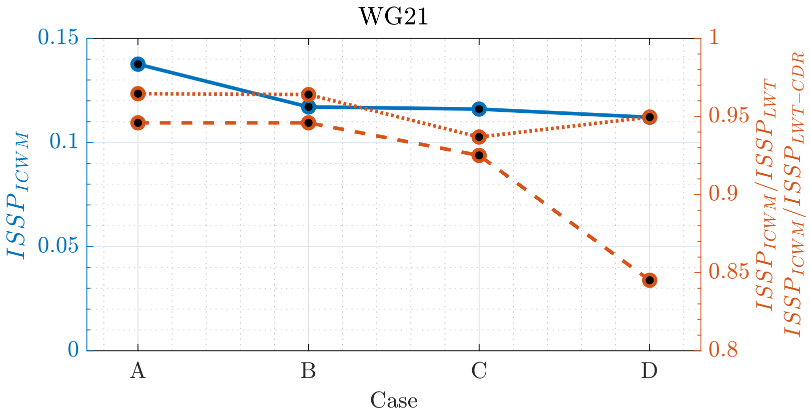

Fig. 17. Improved surface similarity parameter between predicted and measured surface elevations at WG21 (——: ICWM; – – -: ratio of ICWM to LWT; ⋯⋯: ratio of ICWM to LWT-CDR).

Fig. 17 shows the value of ISSP by ICWM and the ratio of ISSP between models for the continuous time series of surface elevation as in the analysis of the wave spectrum. Unlike the results in Figs. 13 and 14 where the linear wave model would be adequate, the improvements by ICWM become more obvious. Additionally, ICWM provides better model performances compared to LWT and LWT-CDR with decreasing directional spreading, while similar patterns in the value of ISSP by ICWM itself are observed for most of the cases reaching a value of about 0.12. The better improvement by ICWM in the case with the smaller directional spreading is believed to be due to the fewer directional components N_θ that were used in the numerical simulation. The more directional wave components the wave field consists of, the smaller the sum of the higher-order of decomposed directional components.

7. Conclusions

This paper has presented the development of real-time phase-resolved wave forecasting by LWT, LWT-CDR, and a Lagrangian model (i.e., ICWM) with unidirectional and multidirectional seas measured by a vessel-mounted instrument. Multidirectional cases require considering the aspects in direction as well as in frequency in order to reach the same model accuracy as in the unidirectional case. Due to the greatly increased computational cost that this involves in multidirectional sea states, real-time prediction in a multidirectional ocean surface becomes a more computationally challenging task compared to in the unidirectional case.

Accordingly, we developed and validated a numerically efficient method in the algorithms for real-time phase-resolved ocean wave prediction. This efficient and simplified approach was derived by neglecting the higher-order terms resulting from the derivative of surface elevation but keeping the other higher-order terms related to the representation of wave surface elevation. The method ensured numerical stability and efficiency in the process of nonlinear assimilation. By using the ensemble-averaged prediction error over the partly overlapping surface samples, we found that the newly-developed method of nonlinear assimilation provides nearly the same model accuracy as the previous one but in a nowcast process that is about more than ten times faster for each wave model. Therefore, the use of numerically efficient assimilation ensures the implementation of all the nonlinear wave models (i.e., ICWM, LWT-CDR) in the real-time system.

We also provided a three-dimensional spatio-temporal prediction zone, in which the measured wave field can be used to describe the future ocean surface prediction, by defining in advance the wave bandwidths in frequency and direction. Because the measurement points are irregularly distributed in space, various boundaries determine the prediction zone. Since they propagate with the maximum or minimum group velocity in the wave propagating angles of each boundary independently, the prediction zone evolves with different shapes and finally disappears when the assimilated information is no longer valid in a prediction. Further, we proved that this prediction zone coincides well with the region where the prediction errors between the predicted and observed wave surfaces remain very small.

Finally, in order to assess the influence of nonlinear properties in Lagrangian surface wave models (i.e., nonlinear phase shift and Stokes drift) for unidirectional sea states as well as multidirectional sea states with different angular spreading, we conducted an experimental campaign designed to construct the multidirectional measurements recorded by an optical system. We showed from the validation of the prediction against the experimental data that the nonlinear phase shift, accounting for wave shape representation and bound waves, is similarly significant in all the cases regardless of the directional spreading. On the other hand, in multidirectional waves, Stokes drift, leading to the nonlinear dispersion relation or nonlinear wave celerity, is probably not as pronounced as in unidirectional waves. This is primarily due to the order of Stokes drift which is higher than that of the nonlinear phase shift. Nevertheless, when it comes to the feed-forward wave-based control strategies for floating offshore wind turbines in the context of the FLOATECH project which require a short time horizon, all the wave models are adequate for real-time prediction. In other words, the algorithms for wave prediction in the present study are found to provide sufficient model accuracy and time horizon in the context of optimal control for floating wind turbines by reference to the previous study (e.g., Ma et al. 2018). However, in the problem of ocean engineering where one necessarily constructs the instantaneous nonlinear wave shape or long-term wave prediction, ICWM, which involves the nonlinear terms, appears to be more attractive for the study of wave propagation whether the case is unidirectional or multidirectional.

CRediT authorship contribution statement

I.-C. Kim: Conceptualization, Methodology, Software, Validation, Writing – original draft. **G. Ducrozet:** Project administration, Conceptualization, Methodology, Investigation, Writing – review & editing, Supervision. **F. Bonnefoy:** Conceptualization, Methodology, Investigation, Writing – review & editing, Supervision. **V. Leroy:** Conceptualization, Methodology, Investigation, Writing – review & editing, Supervision. **Y. Perignon:** Project administration, Conceptualization, Methodology, Investigation, Writing – review & editing, Supervision.

Declaration of competing interest

The authors declare that they have no known competing financial interests or personal relationships that could have appeared to influence the work reported in this paper.

Data availability

Data such as experimental datasets and prediction results are openly available at https://doi.org/10.5281/zenodo.7689781 repository.

Acknowledgments

This work was done within the framework of the European H2020 FLOATECH project, Grant agreement ID: 101007142. The authors acknowledge the support of the French Agence Nationale de la Recherche (ANR), under grant ANR-20-CE05-0039 (project CREATIF). The authors also thank the experimental team at LHEEA/Centrale Nantes-CNRS that contributed to the experimental campaign and the corresponding database.

Appendix. Assimilation for LWT-CDR

As we illustrated the assimilation methods for ICWM, we present the two assimilation formulations (i.e., previous and simplified ones) for LWT-CDR in this appendix. The previous assimilation equations of Desmars et al. (2020) are given:

$$\begin{gathered}
A_{(m,n)}^{LWT-CDR} = \sum_{l=1}^{L} \cos\tilde{\psi}_{nl} P_{ml}^{LWT-CDR},\ A_{(m,N+n)}^{LWT-CDR} = \sum_{l=1}^{L} \sin\tilde{\psi}_{nl} P_{ml}^{LWT-CDR} \\
A_{(N+m,n)}^{LWT-CDR} = \sum_{l=1}^{L} \cos\tilde{\psi}_{nl} Q_{ml}^{LWT-CDR},\ A_{(N+m,N+n)}^{LWT-CDR} = \sum_{l=1}^{L} \sin\tilde{\psi}_{nl} Q_{ml}^{LWT-CDR} \\
B_{m}^{LWT-CDR} = \sum_{l=1}^{L} \bar{\eta}_l P_{ml}^{LWT-CDR},\ B_{N+m}^{LWT-CDR} = \sum_{l=1}^{L} \bar{\eta}_l Q_{ml}^{LWT-CDR}
\end{gathered} \tag{A.1}$$

with

$$\begin{aligned}
P_{ml}^{LWT-CDR} &= \cos\tilde{\psi}_{ml} + (a_m \sin\tilde{\psi} - b\cos\tilde{\psi}) k_m^2 a_m \omega_m t_l \\
Q_{ml}^{LWT-CDR} &= \sin\tilde{\psi}_{ml} + (a_m \sin\tilde{\psi} - b\cos\tilde{\psi}) k_m^2 b_m \omega_m t_l
\end{aligned} \tag{A.2}$$

Eq. (A.1) are simplified into Eq. (A.3) to derive the simplified assimilation for LWT-CDR (referred to as LWT-CDR-S) by discarding the terms which are at a higher order than $O(1)$ in P and Q:

$$\begin{gathered}
A_{(m,n)}^{LWT-CDR-S} = \sum_{l=1}^{L} \cos\tilde{\psi}_{nl} P_{ml}^{LWT},\ A_{(m,N+n)}^{LWT-CDR-S} = \sum_{l=1}^{L} \sin\tilde{\psi}_{nl} P_{ml}^{LWT} \\
A_{(N+m,n)}^{LWT-CDR-S} = \sum_{l=1}^{L} \cos\tilde{\psi}_{nl} Q_{ml}^{LWT},\ A_{(N+m,N+n)}^{LWT-CDR-S} = \sum_{l=1}^{L} \sin\tilde{\psi}_{nl} Q_{ml}^{LWT} \\
B_{m}^{LWT-CDR-S} = \sum_{l=1}^{L} \bar{\eta}_l P_{ml}^{LWT},\ B_{N+m}^{LWT-CDR-S} = \sum_{l=1}^{L} \bar{\eta}_l Q_{ml}^{LWT}
\end{gathered} \tag{A.3}$$

References

Al-Ani, M., Belmont, M., Christmas, J., 2020. Sea trial on deterministic sea waves prediction using wave-profiling radar. Ocean Eng. 207, 107297.

Belmont, M., Horwood, J., Thurley, R., Baker, J., 2007. Shallow angle wave profiling lidar. J. Atmos. Ocean. Technol. 24 (6), 1150–1156.

Blondel, E., Bonnefoy, F., Ferrant, P., 2010. Deterministic non-linear wave prediction using probe data. Ocean Eng. 37 (10), 913–926.

Bonnefoy, F., Delacroix, S., Ducrozet, G., Kim, I., Leroy, V., 2023. FLOATECH Project Database. Zenodo, http://dx.doi.org/10.5281/zenodo.7689781, Funded by European Commission, project FLOATECH, grant 101007142.

Booij, N., Ris, R.C., Holthuijsen, L.H., 1999. A third-generation wave model for coastal regions: 1. Model description and validation. J. Geophys. Res.: Oceans 104 (C4), 7649–7666.

Calvetti, D., Reichel, L., Shuibi, A., 2004. L-curve and curvature bounds for Tikhonov regularization. Numer. Algorithms 35 (2), 301–314.

Dannenberg, J., Hessner, K., Naaijen, P., van den Boom, H., Reichert, K., 2010. The on board wave and motion estimator OWME. In: The Twentieth International Offshore and Polar Engineering Conference. OnePetro, pp. 424–431.

Desmars, N., Bonnefoy, F., Grilli, S., Ducrozet, G., Perignon, Y., Guérin, C.A., Ferrant, P., 2020. Experimental and numerical assessment of deterministic nonlinear ocean waves prediction algorithms using non-uniformly sampled wave gauges. Ocean Eng. 212, 107659.

Desmars, N., Pérignon, Y., Ducrozet, G., Guérin, C.A., Grilli, S.T., Ferrant, P., 2018. Phase-resolved reconstruction algorithm and deterministic prediction of nonlinear ocean waves from spatio-temporal optical measurements. In: International Conference on Offshore Mechanics and Arctic Engineering, Vol. 51272. American Society of Mechanical Engineers, p. V07BT06A054.

Grilli, S.T., Guérin, C.A., Goldstein, B., 2011. Oceanwave reconstruction algorithms based on spatio-temporal data acquired by a flash LiDAR camera. In: The Twenty-First International Offshore and Polar Engineering Conference. OnePetro, pp. 275–282.

Guérin, C.A., Desmars, N., Grilli, S.T., Ducrozet, G., Perignon, Y., Ferrant, P., 2019. An improved Lagrangian model for the time evolution of nonlinear surface waves. J. Fluid Mech. 876, 527–552.

Hansen, P.C., 2000. The L-curve and its use in the numerical treatment of inverse problems. In: Computational Inverse Problems in Electrocardiology. WIT Press, pp. 119–142.

Hilmer, T., Thornhill, E., 2015. Observations of predictive skill for real-time deterministic sea waves from the WaMoS II. In: OCEANS 2015-MTS/IEEE Washington. IEEE, pp. 1–7.

Janssen, T., Herbers, T., Battjes, J., 2006. Generalized evolution equations for nonlinear surface gravity waves over two-dimensional topography. J. Fluid Mech. 552, 393–418.

Kabel, T., Georgakis, C.T., Zeeberg, A.R., 2019. Mapping ocean waves using new LIDAR equipment. In: Proceedings of the Twenty-Ninth (2019) International Ocean and Polar Engineering Conference. nternational Society of Offshore and Polar Engineers, pp. 2258–2562.

Klein, M., Dudek, M., Clauss, G.F., Ehlers, S., Behrendt, J., Hoffmann, N., Onorato, M., 2020. On the deterministic prediction of water waves. Fluids 5 (1), 9.

Köllisch, N., Behrendt, J., Klein, M., Hoffmann, N., 2018. Nonlinear real time prediction of ocean surface waves. Ocean Eng. 157, 387–400.

Kusters, J., Cockrell, K., Connell, B., Rudzinsky, J., Vinciullo, V., 2016. FutureWaves™: A real-time ship motion forecasting system employing advanced wave-sensing radar. In: OCEANS 2016 MTS/IEEE Monterey. IEEE, pp. 1–9.

Li, G., Weiss, G., Mueller, M., Townley, S., Belmont, M.R., 2012. Wave energy converter control by wave prediction and dynamic programming. Renew. Energy 48, 392–403.

Ma, Y., Sclavounos, P.D., Cross-Whiter, J., Arora, D., 2018. Wave forecast and its application to the optimal control of offshore floating wind turbine for load mitigation. Renew. Energy 128, 163–176.

Mitsuyasu, H., Tasai, F., Suhara, T., Mizuno, S., Ohkusu, M., Honda, T., Rikiishi, K., 1975. Observations of the directional spectrum of ocean WavesUsing a cloverleaf buoy. J. Phys. Oceanogr. 5 (4), 750–760.

Naaijen, P., Trulsen, K., Blondel-Couprie, E., 2014. Limits to the extent of the spatio-temporal domain for deterministic wave prediction. Int. Shipbuild. Prog. 61 (3–4), 203–223.

Naaijen, P., Van Oosten, K., Roozen, K., van't Veer, R., 2018. Validation of a deterministic wave and ship motion prediction system. In: International Conference on Offshore Mechanics and Arctic Engineering, Vol. 51272. American Society of Mechanical Engineers, p. V07BT06A032.

Nouguier, F., Chapron, B., Guérin, C.A., 2015. Second-order Lagrangian description of tri-dimensional gravity wave interactions. J. Fluid Mech. 772, 165–196.

Nouguier, F., Grilli, S.T., Guérin, C.A., 2013. Nonlinear ocean wave reconstruction algorithms based on simulated spatiotemporal data acquired by a flash LIDAR camera. IEEE Trans. Geosci. Remote Sens. 52 (3), 1761–1771.

Nouguier, F., Guérin, C.A., Chapron, B., 2009. "Choppy wave" model for nonlinear gravity waves. J. Geophys. Res.: Oceans 114 (C9).

Nouguier, F., Guérin, C.A., Chapron, B., 2010. Scattering from nonlinear gravity waves: The "choppy wave" model. IEEE Trans. Geosci. Remote Sens. 48 (12), 4184–4192.

Perlin, M., Bustamante, M.D., 2016. A robust quantitative comparison criterion of two signals based on the Sobolev norm of their difference. J. Eng. Math. 101 (1), 115–124.

Pierson, Jr., W.J., 1961. Models of Random Seas Based on the Lagrangian Equations of Motion. Technical Report, New York Univ Bronx School of Engineering and Science.

Pierson, Jr., W.J., Moskowitz, L., 1964. A proposed spectral form for fully developed wind seas based on the similarity theory of SA Kitaigorodskii. J. Geophys. Res. 69 (24), 5181–5190.

Previsic, M., Karthikeyan, A., Lyzenga, D., 2021. In-ocean validation of a deterministic sea wave prediction (DSWP) system leveraging X-band radar to enable optimal control in wave energy conversion systems. Appl. Ocean Res. 114, 102784.

Qi, Y., Wu, G., Liu, Y., Kim, M.H., Yue, D.K., 2018a. Nonlinear phase-resolved reconstruction of irregular water waves. J. Fluid Mech. 838, 544–572.

Qi, Y., Wu, G., Liu, Y., Yue, D.K., 2018b. Predictable zone for phase-resolved reconstruction and forecast of irregular waves. Wave Motion 77, 195–213.

Wijaya, A.P., Naaijen, P., van Groesen, E., et al., 2015. Reconstruction and future prediction of the sea surface from radar observations. Ocean Eng. 106, 261–270.

Willmott, C.J., 1982. Some comments on the evaluation of model performance. Bull. Am. Meteorol. Soc. 63 (11), 1309–1313.

Wu, G., 2004. Direct Simulation and Deterministic Prediction of Large-Scale Nonlinear Ocean Wave-Field (Ph.D. thesis). Massachusetts Institute of Technology.

Zhang, C., Chen, Z., Zhao, C., Chen, X., Wei, Y., He, J., 2022. Deterministic sea wave prediction based on least squares with regularization algorithm using coherent microwave radar. IEEE Trans. Geosci. Remote Sens.